UNIVERSITY OF COPENHAGEN
FACULTY OF SCIENCE

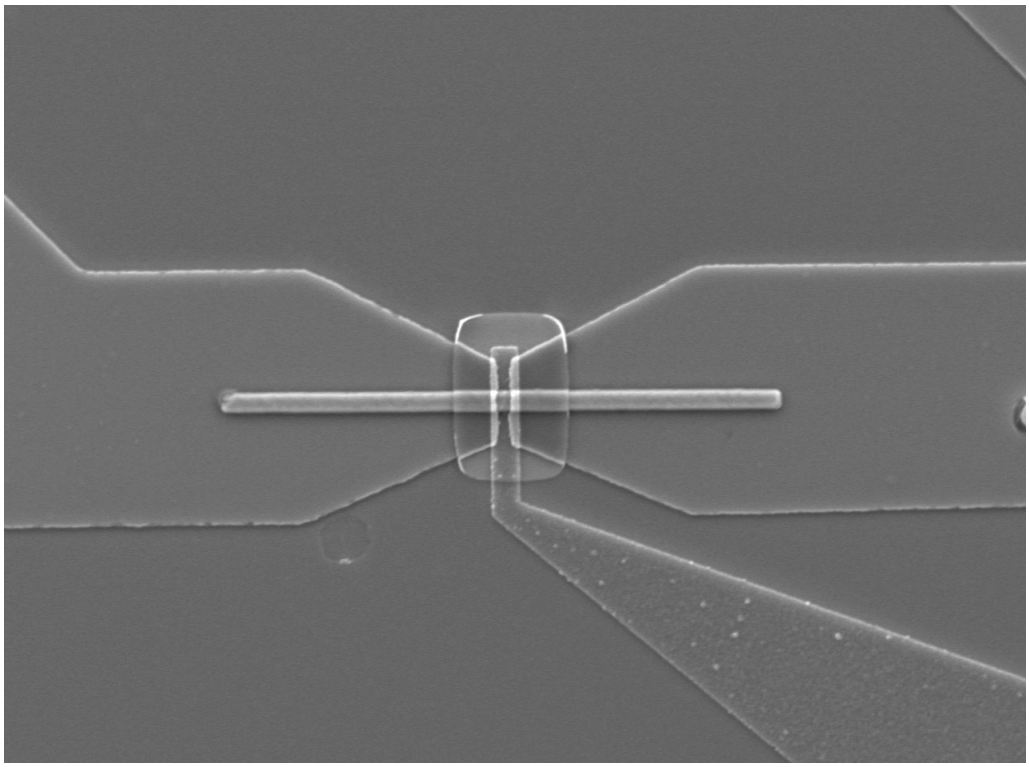

Master Thesis

Laurits Orheim Andersen

Superconducting Qubits Based on Semiconductor Two Dimensional Electron Gases and Selective Area Grown Nanowires

Advisor: Karl David Petersson

Handed in: October 17, 2018

Abstract

Superconducting qubits based on voltage tuneable superconductor-semiconductor Josephson junctions called gatemons could be used to realize a universal quantum computer. Before this can be realized, two challenges must be overcome; the coherence times of the qubits must be longer, and fabrication must be deterministic.

This thesis presents the nanofabrication and characterization of two gatemon qubit devices based on different materials. In one the Josephson junction is based on a proximitized two dimensional electron gas. The other device is based on nanowires grown directly on the substrate using selective area growth.

The lifetimes and coherence times for these devices are extracted, finding $T_1 = 2.77\mu$s and $T_2* = 359$ns for the first device and $T_1 = 180$ns for the second device with the coherence time being too short to measure.

Contents

1 Introduction **3**

1.1 Overview 6

2 Superconducting qubits and circuit QED **8**

2.1 The quantum LC oscillator 8

2.2 The Josephson junction 9

2.3 Superconducting qubits 10

2.3.1 The Cooper pair box 10

2.3.2 The gatemon qubit 11

2.4 Sources of decoherence 15

2.5 The Jaynes-Cummings model 16

2.5.1 Dispersive readout 18

2.6 Gates 19

2.6.1 Single qubit rotations 19

2.6.2 Two qubit gates 20

3 Measurement setup **22**

3.1 The dilution refrigerator 22

3.2 Room temperature electronics 26

4 The sample **28**

4.1 Design 28

4.2 Materials 30

4.2.1 2DEG 30

4.2.2 SAG 30

4.3 Fabrication 32
4.3.1 2DEG 33
4.3.2 SAG 35

5 Measurements 41
5.1 Initial tuneup 41
5.1.1 Lifetime and coherence time measurements 43
5.2 Results 45
5.2.1 2DEG 45
5.2.2 SAG 47
5.3 Discussion 50

6 Conclusions and lookout 53

A SAG based gatemon fabrication recipe 60
A.1 Al etch 60
A.2 Gate dielectric 61
A.3 Top Gate 62

B 2DEG based gatemon fabrication recipe 63
B.1 Alignemnt marks 63
B.2 Nanowire mesa etch 64
B.3 Microwave control 65
B.4 Josephson junction 66
B.5 ALD 67
B.6 Gates 67
B.7 Contacts 68

Chapter 1

Introduction

When quantum mechanical degrees of freedom are used to represent and process data, information processing fundamentally different from its classical analogue is possible. This opens up to a number of different possible applications such as quantum communication, analogue quantum simulation, and universal quantum computing, or simply, quantum computing, which is the focus this thesis.

A classical computer functions by processing bits of information by applying a set of logic gates. A quantum computer processes quantum bits (qubits) by applying quantum gates to the qubits [31], and at the end performing a measurement of the state of the qubits. The state of a system consisting of n classical bits can be described by an n-digit binary number. The quantum state of an n qubit system on the other hand needs $2^n - 1$ complex numbers to completely describe the system.

A number of quantum algorithms that outperform classical algorithms have been found, including Shor's algorithm and Grover's algorithm, which are especially interesting as they solve problems that are very general. Grover's algorithm is an algorithm for searching an unsorted database where the time it takes to run the algorithm scales as the square root of the number of entries in the database [32]. The best classical algorithm involves checking at least some fraction of the entries and in the worst case all of them, and therefore the search time scales linearly with the size of the database. Shor's algorithm solves the problem of finding the prime factors of a number N [32]. The time it takes for Shor's algorithm is polynomial in N, while the time taken for the fastest known classical general

factorization algorithm is greater than polynomial time [24]. The fact that multiplying primes together is computationally easy while finding the prime factors of a number is computationally hard is what make some asymmetric encryption algorithms such as the widely used RSA algorithm secure. This means that such encryption schemes would no longer be secure with quantum computers around.

To determine whether a given physical system is suitable to be used as the basis for a quantum computer, the DiVincenzo criteria [12] can be used. These are five requirements the system must fulfill to be a platform for building a quantum computer, plus an additional two requirements for quantum communication. The five main requirements are as follows:

A scalable physical system with well characterized qubits. That a qubit is well characterized means it is a physical system where the parameters describing the qubit and how it interacts with other qubits and the environmentare well understood. It is important that the qubits have quantum states that can be used as a computational basis. It is also important that it is possible to scale up the number of qubits.

The ability to initialize the state of the qubits to a simple fiducial state, such as $|000...\rangle$ Before the start of computation it is necessary to be in a known state. Furthermore, certain algorithms such as quantum error correction require qubit reset on the fly.

Long relevant decoherence times, much longer than the gate operation time. Any quantum system coupled to its environment will decohrere on some timescale called the decoherence time. Decoherence wan be seen as loss of information to the environment, and is therefore detrimental to computation. If quantum error correction is used, some amount of decoherence is tolerable, and can be corrected as the algorithm is running. This means that the decoherence time need not be long compared to the length of the algorithm, but to the time of gate operation.

A "universal" set of quantum gates. A quantum computer must be able to simulate any unitary evolution of the qubits to arbitrary precision from a finite set of gates. A set of gates which fulfills this requirement is called a universal gate set.

An example of this is being able to do the controlled-NOT gate between any pair of qubits combined with single qubit rotations.

A qubit-specific measurement capability. After computation the resulting state of the qubits must be read out. That the measurement is qubit specific means that the state of individual qubits is what is measured rather than a collective property. Qubit specific measurement is needed for error correction.

Many physical systems that meet these criteria have been proposed and explored experimentally. Leading technologies at the moment are trapped ion qubits formed by the electronic states of ions trapped with electromagnetic fields and superconducting qubits formed by the energy levels of quantized electrical circuits.

Superconducting qubits, which are the qubits explored in this thesis, have reached coherence times in excess of $100\ \mu$s [14] and one and two gate fidelities in excess of 99% approaching what is required for quantum error correction [1].

The standard way for controlling the transition frequency of a superconducting qubit is to thread a magnetic flux through a SQUID loop containing the Josephson junction. The devices studied in this thesis are based on Josephson junctions that can be tuned with an electrostatic gate. This type of superconducting qubit is called a gatemon [23]. A potential advantage of this type of device is that on chip voltage signals may be easier to screen from one another than the currents needed for flux control. This means that cross talk between qubits could be manged more easily using this approach. Voltage control also means that no DC currents are needed, which means less dissipation in resistive lines in the dilution refrigerator. Finally, the electrostatic gate also allows z-control and Rabi pulses to be combined on a single line.

The first version of the gatemon was based on a junction made with nanowire grown by the vapor–liquid–solid (VLS) medhod which was transferred on to the substrate [23]. This method of fabrication is not deterministic, and usually requires modification of the device layout around the nanowire. To solve this problem a new type of qubit with a junction based on a two dimensional electron gas was introduced [8]. This two dimensional electron gas (2DEG) is grown on an

InP substrate on which is therefore what is used for the whole chip including the qubit island and transmission line resonators on the chip.

It was suspected, that the lifetimes of the 2DEG based gatemon qubit was limited by dielectric losses in the InP substrate [8]. This lead us to investigate a new type of device based on selective area growth (SAG), which allows growth of horizontal nanowires directly on the substrate and could be implemented on a silicon substrate.

In this thesis gatemon qubits made using the 2DEG and a version of SAG gatemon qubits on InP are fabricated and measured. InP was used as a substrate for these qubits for these devices to test the concept before moving to SAG on Si.

The fabrication process for the 2DEG device was developed in collaboration with Malcolm Connolly. I worked together with Albert Hertel on the fabrication and process development for the SAG device. The fridge upgrade was done together with Albert Hertel and Malcolm Connolly. Natalie Pearson helped out with the electronics and software for the measurements. Measurements on the SAG device were done together with Albert Hertel.

1.1 Overview

This thesis presents the theoretical framework for describing superconducting qubits coupled to transmission line resonators, and explains gate tuneable superconducting qubits called gatemons.

The setup used for characterizing these devices is then explained going through both what is inside the dilution refrigerator and the control electronics at room temperature.

The next chapter goes through the design, materials, and fabrication used to make these devices. Here the individual fabrication steps for the two devices are explained.

Measurement techniques for characterizing the devices with continuous wave spectroscopy and pulse schemes to measure qubit lifetime and coherence time is explained. The measurement results are then presented.

Finally these results are summarized and discussed together with what could

be done to further improve these devices.

Chapter 2

Superconducting qubits and circuit QED

Circuit quantum electrodynamics (circuit QED) is the framework for engineering superconducting quantum circuits capable of control and readout of superconducting qubits. Circuit QED allows us to use circuit elements such as inductors and capacitors that can be fabricated on a chip to build qubits and resonators.

The systems in circuit QED are analogous to the systems in cavity QED where atoms are placed inside high Q optical cavities to enhance the light-matter interaction, similarly, in circuit QED "artificial atom" qubits are coupled to microwave resonators to control and readout the state of the qubit.

2.1 The quantum LC oscillator

To analyze parallel circuit of a capacitor with capacitance C and an inductor with inductance L, we take as a starting point the Hamiltonian for the system written in terms of the charge on the capacitor $\hat{Q}$ and the flux in the inductor $\hat{\Phi}$,

$$\hat{H} = \frac{\hat{Q}^2}{2C} + \frac{\hat{\Phi}^2}{2L}. \tag{2.1}$$

The first term is associated with the electric potential energy of the capacitor while the second comes from the magnetic energy of the inductor. The charge and flux

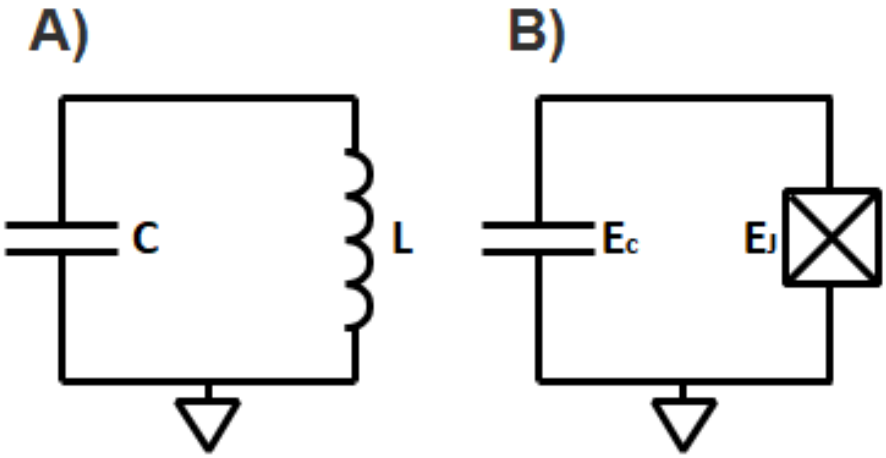

Figure 2.1: A) A parallel LC circuit. This circuit behaves like a harmonic oscillator. B) A superconducting qubit. The circuit is the came as the previous, but with the inductor replaced by a Josephson junction which acts as a nonlinear inductance. The Josephson junction is represented by a square with an x in it (⊠)

.

are conjugate variables obeying

$$\left[\hat{\Phi}, \hat{Q}\right] = i\hbar, \tag{2.2}$$

and therefore we recognize the system as a harmonic oscillator with frequency $\omega = \frac{1}{\sqrt{LC}}$.

2.2 The Josephson junction

The Josephson junction (JJ) consists of two superconductors connected by a weak link [18]. The weak link can be for example a normal metal (superconductor normal superconductor, or SNS) or an insulator (SIS) where the length of the weak, L, link is short compared to the superconducting coherence length $\xi_0 \gg L$. For a JJ in the tunnel limit, when no voltage is applied a supercurrent I will flow between the two superconductors according to

$$I = I_c \sin\phi, \tag{2.3}$$

where ϕ is the difference in the phase of the superconducting order parameter across the junction and I_c is called the critical current. If a voltage across the junction V is applied, the phase will evolve according to

$$\frac{d\phi}{dt} = \frac{2\pi}{\Phi_0}V, \tag{2.4}$$

where $\Phi_0 = \frac{h}{2e}$ is the magnetic flux quantum. For a Josephson junction we can define a Josephson inductance we will call L_J. To do this we first take the total derivative of the supercurrent with respect to time using equations (2.3) and (2.4) we get

$$\frac{dI}{dt} = I_c \cos(\phi)\frac{2\pi}{\Phi_0}V. \tag{2.5}$$

If we remember that for an inductor $V = L\frac{dI}{dt}$ we can define a nonlinear inductance for the JJ as follows

$$L_J = \frac{\Phi_0}{2\pi I_c \cos(\phi)}. \tag{2.6}$$

The JJ is the only circuit element that is both nonlinear and non-dissipative, which is why it is useful for building qubits.

2.3 Superconducting qubits

2.3.1 The Cooper pair box

To build a qubit it is necessary to have two levels that can form the computational basis. Since the LC oscillator has equally spaced energy levels it is impossible to only drive the transition between the ground state and the first excited state without also driving the transition from the first excited state to the second and so on. To solve this the Josephson junction replaces the inductor to introduce nonlinearity to the circuit.

The simplest superconducting qubit is the Cooper pair box (CPB) [16]. It consists of a superconducting qubit island connected through a JJ to a reservoir. The CPB can be modelled as a capacitor and JJ connected in parallel. The Hamiltonian for this circuit is then the same as in (2.1) but with the Josephson inductance from (2.6) replacing the inductance. The Hamiltonian can be written in terms of

the characteristic energies $E_J = \frac{I_c \Phi_0}{2\pi}$ called the Josephson energy associated with a supercurrent flowing through the junction, and $E_c = \frac{e^2}{2C}$ called the charging energy, which is the energy it takes to move an electron from the reservoir to the qubit island. The Hamiltonian is

$$\hat{H} = 4E_c(\hat{n} - n_g)^2 - E_J \cos\left(\hat{\phi}\right) \tag{2.7}$$

where $\hat{n}$ is the cooper pair number operator, and n_g the gate charge induced by an electrostatic gate by tuning the gate voltage.

Fluctuations in the electric environment of the qubit enter through the term n_g and cause dechoerence. When the dominating energy scale is the charging energy, meaning $E_c \gg E_j$, an approach to minimize the coupling to charge noise is to operate the qubit at a charge degeneracy point, which is a point in gate charge where the charge states $|n\rangle$ and $|n+1\rangle$ have the same charging energy and the qubit is first order insensitive to charge noise. These charge degeneracy points are the points where the $n_g = -0.5, 0.5, 1.5....$

Another approach to reduce the sensitivity to charge noise is to operate the CPB in what is known as the transmon regime where the Josephson energy dominates $E_J \gg E_c$. In this regime the qubit is known as a transmon [20]. Going into the transmon regime has a disadvantage; the anhamonicity of the qubit is reduced when $\frac{E_J}{E_c}$ is increased. A lower anharmonicity means that the pulses used to control the qubit must have a smaller bandwidth to avoid driving the higher transitions in the qubit, and this sets a limit of the pulse length. The anharmonicity is defined as $\alpha = E_{12} - E_{01}$, and in the transmon regime this goes as $\alpha \approx -E_c$.

2.3.2 The gatemon qubit

In order to control the qubits a mechanism to tune E_J is usually included by introducing a Superconducting Quantum Interference Device (SQUID) which is a loop with two JJs in it. This enables tuneability of the transmon by threading a flux through the loop using for example flux bias lines.

To tune E_J the gatemon uses a superconductor-semiconductor-superconductor (S-Sm-S) JJ with an electrostatic gate near the junction region. This approach allows one to tune the charge density in the semiconductor region with electric

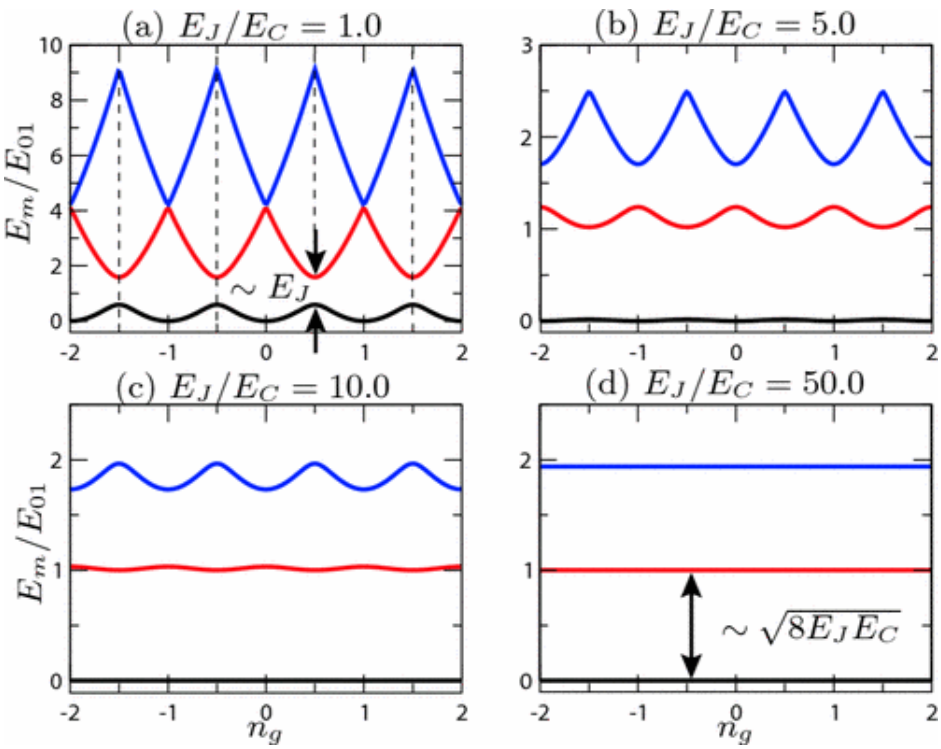

Figure 2.2: From [20], numerical solutions to the eigenenergies of the CPB Hamiltonian. The energies of the first three energy levels are plotted against the gate charge for different values of $\frac{E_J}{E_c}$. It can be seen how increasing the ratio $\frac{E_J}{E_c}$ flattens the charge dispersion.

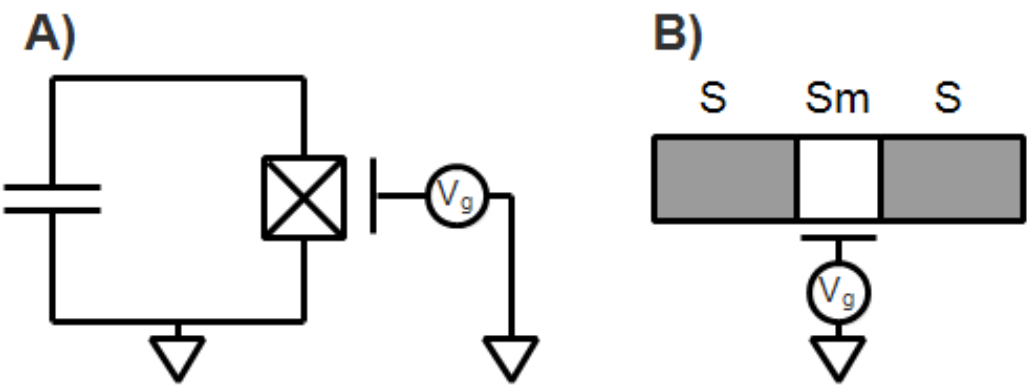

Figure 2.3: A) Schematic illustration of a gatemon qubit with the Josephson energy tuned by the voltage V_g. B) Illustration of the superconductor-semiconductor-superconductor Josephson junction, where the electrostatic gate can tune the charge density in the junction region, and therefore the critical current.

field effect, thus changing the number of channels and their transmission, which changes the critical current I_c and therefore also the Josephson energy E_J, which is linear in I_c. This approach uses voltages rather than currents to control the qubit frequency which depends.

The first version of the gatemon qubit was based on a Josephson junction formed by a semiconductor nanowire coated with epitaxially grown aluminium, that through the proximity effect induces superconductivity in the semiconductor. The aluminium was etched away in a segment of the nanowire forming a S-Sm-S junction in the nanowire [23]. A later version of the gatemon was based on a proximitized two-dimensional electron gas [8]. This version was developed to avoid having to transfer grown nanowires on a substrate, which is not a deterministic and therefore not an easily scaleable approach.

The superconducting proximity effect is a phenomenon that arises when a superconductor and a semiconductor come into electrical contact [30]. When this happens Cooper pairs from the superconductor can enter the semiconductor and induce superconductivity at the interface with the superconductor. The interface between Al and InAs grown by molecular beam epitaxy can be grown in a way that makes it impurity free, so a hard superconducting gap is induced in the InAs[9].

In the S-Sm-S JJ, the relationship between the current and the phase is different form Equation 2.3. In the short junction limit where the superconducting coherence length is much longer than the coherence length in the junction $\xi \gg L$, transport across the junction occurs through Andreev bound states, each with transmission T_i [4]. Andreev reflection is a process that occurs when an electron in the semiconductor is incident on the interface with the superconductor at energy less than the energy gap Δ. The incident electron forms a cooper pair with another electron when entering the superconductor, and a hole with the same momentum and opposite spin is retroreflected. The same can occur with an incident hole and a retroreflected electron. Multiple Andreev reflections at the two interfaces result in Andreew bound states. Each Andreev bound state has ground state energy $-\Delta\sqrt{1 - T_i \sin\left(\hat{\phi}/2\right)}$. Summation over the individual channels gives the junction potential

$$V(\hat{\phi}) = -\Delta \sum_i \sqrt{1 - T_i \sin\left(\hat{\phi}/2\right)}. \tag{2.8}$$

With this potiential replacing the term $-E_j \cos\left(\hat{\phi}\right)$ in Equation 2.7, the anharmonicity can be approximated as [21]

$$\alpha \approx -E_c(1 - \frac{3\sum_i T_i^2}{4\sum_i T_i}). \tag{2.9}$$

In the tunnel limit $T_i \to 0$ the result $\alpha \approx -E_c$ for the S-I-S junction is recovered, while in the other limit $T_i \to 0$ the anharmonicity is reduced to $\alpha \approx -\frac{1}{4}E_c$. Measurements of the anharmonicity of in a nanowire gatemon have been carried out showing roughly half the anharmonicity and indicating that three or fewer channels contribute to transport through the junction [21].

The short junction limit is only approximately valid since the junction coherence length is $\xi = \sqrt{\xi_0 l}$ where $l \approx 100$ nm [21] is the mean free path in the junction and $\xi_0 = 1600$ nm the superconducting coherence lenght of Al [18], which gives $\xi = 400$ nm while the typical junction length is on the order of 200nm. Beyond this approximation, the spectrum of the Andreev bound states takes on a more complicated form [36].

In this work we develop qubits with a JJ based on nanowires grown by a method called selective area growth. This method allows us to grow horizontal nanowires at specified locations on the substrate. This approach solves the problem of scaleability, and it can be implemented on silicon substrates, which has been shown to be able to support low loss transmission line resonators [5]. Switching to Si substrates could reduce the dielectric losses and improve the qubit lifetimes directly since the qubit itself has a capacitor and through a reduced Purcell decay rate [34].

2.4 Sources of decoherence

Dielectric loss due to coupling to resonant two level systems with a dipole moment has been shown to be a dominant contributor to relaxation in superconducting qubits [29]. For this reason the materials chosen to fabricate the qubits need to have a low dielectric loss tangent, which is relevant when choosing substrates and dielectrics for fabrication.

A finite subgap conductance in the the JJ can be modelled as an added parallel resistor in the CPB circuit, and this will lead to loss similar to the classical RC decay time of this circuit. A higher subgap conductance has been correlated with a lower qubit lifetime in superconducting qubits [19].

Quasiparticle excitations in the junction can change E_J which will change the qubit frequency causing decoherence. An Andreev bound state in the junction has energy $\pm\Delta\sqrt{1 - T_i \sin\left(\hat{\phi}/2\right)}$. This means that in these qubits that operate around $\phi = 0$, the energy it takes to excite a quasiparticle in the junction is 2Δ. If qubit transition frequency is near 2Δ quasiparticle excitations in the JJ can lead to dechoherence [28].

Fluctuations in the charge environment of the qubit are another cause for decoherence and have also been discussed in Section 2.3.2. Microscopic two level fluctuations cause noise in the charge environment which couples to n_g [17] and in these qubits also E_j due to field effect in the semiconductor JJ. Noise from the electrostatic gate also couples to the qubit frequency, which is why filtering and attenuation of the control lines is important.

2.5 The Jaynes-Cummings model

The Jaynes-Cummings model is often used in quantum optics to model the situation where an atom interacts with a mode of an optical cavity [15]. To read out the state of a superconducting qubit it is coupled to a transmission line resonator, and we model this coupled system with the Jaynes-Cummings model. In the cQED system the gatemon qubit plays the role of the atom and the transmission line resonator plays the role of the cavity.

In section 2.1, we saw that an LC oscillator is a harmonic oscillator. For the LC oscillator we can therefore write the Hamiltonian as

$$\hat{H}_r = \hbar\omega_r(\hat{a}^\dagger\hat{a} + 1/2) \tag{2.10}$$

Where $\hat{a}$ and $\hat{a}^\dagger$ are the raising and lowering operators, and ω_r is the resonance frequency of the fundamental mode of the transmission line oscillator. The qubit is approximated as a two level system, with the Hamiltonian

$$\hat{H}_q = \frac{\hbar}{2}\omega_q\hat{\sigma}_z, \tag{2.11}$$

where ω_q is the qubit frequency and $\hat{\sigma}_z$ is a Pauli operator. Capacitively coupling the end of the transmission line resonator to the qubit island adds a coupling term to the Hamiltonian which is

$$\hat{H}_c = \hbar g\hat{\sigma}_x(\hat{a}^\dagger + \hat{a}) \tag{2.12}$$

where g is the qubit-resonator coupling strength. In the rotating wave approximation (RWA) we can throw away the terms with $\hat{a}^\dagger\hat{\sigma}_+$ and $\hat{a}\hat{\sigma}_-$ giving us the Jaynes-Cummings Hamiltonian

$$\hat{H}_{JC} = \frac{\hbar\omega_q}{2}\hat{\sigma}_z + \hbar\omega_r(\hat{a}^\dagger\hat{a} + 1/2) + \hbar g(\hat{a}^\dagger\sigma_- + \hat{a}\sigma_+). \tag{2.13}$$

The last term in this Hamiltonian allows an excitation to be transferred from the qubit to the resonator or from the resonator to the qubit. When the qubit and the cavity are on resonance, meaning $\omega_q = \omega_r$, the energy levels form the Jaynes-Cummings ladder seen in Figure 2.4. The splitting between the states $(|1,g\rangle + |0,e\rangle)/\sqrt{2}$ and $(|1,g\rangle - |0,e\rangle)/\sqrt{2}$ is called the vacuum Rabi splitting, since the

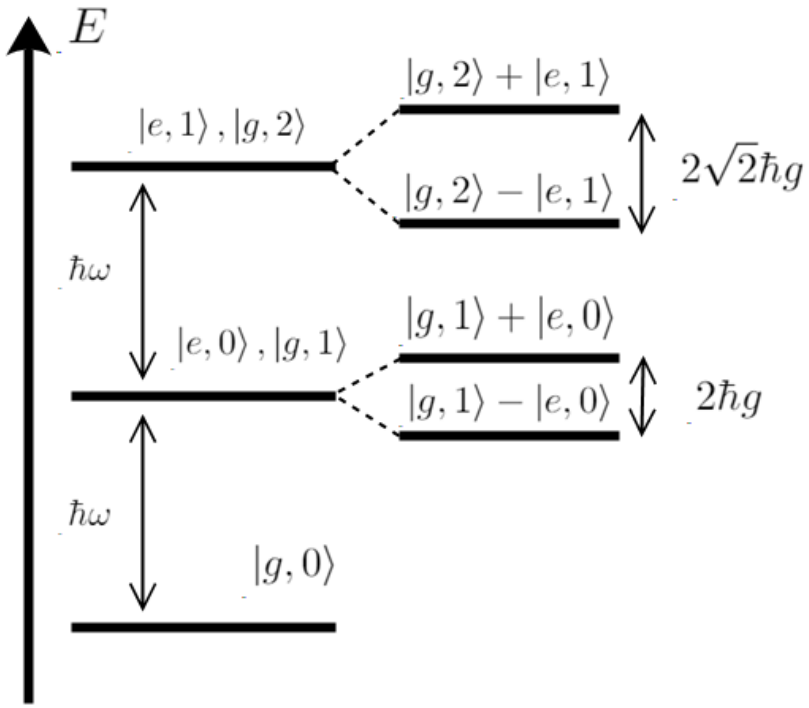

Figure 2.4: The Jaynes-Cummings laddder. On the left are the energy levels of the resonator. On the right the energy levels of the hybridized qubit-resonator system on resonance($\omega_r = \omega_q = \omega$).

qubit undergoes rabi oscillations stimulated by the vacuum state of the resonator. The vacuum Rabi splitting $2\hbar g$ can be observed when the linewidths of the qubit and the resonator are less than g.

In the regime called the dispersive regime where the qubit and resonator are far detuned from each other, which means that $\omega_q - \omega_r = \Delta \gg g$, another approximation can be made to the Jaynes-Cummings Hailtonian. One can expand the Hamiltoninan for the qubit-resonator system in the parameter g/Δ to second order and afterwards make the two level qubit approximation. The resulting Hamiltonian is

$$\hat{H}_{JCd} = \frac{\hbar\omega_q'}{2}\hat{\sigma}_z + \hbar\hat{a}^\dagger\hat{a}\omega_r' + \hbar\hat{a}^\dagger\hat{a}\chi\hat{\sigma}_z. \tag{2.14}$$

The quantities ω_q' and ω_r' are the resonator and qubit frequencies shifted by the Lamb shift. The last term can be interpreted as either a shift of the qubit frequency depending on the photon number in the cavity, or a shift of the cavity resonance

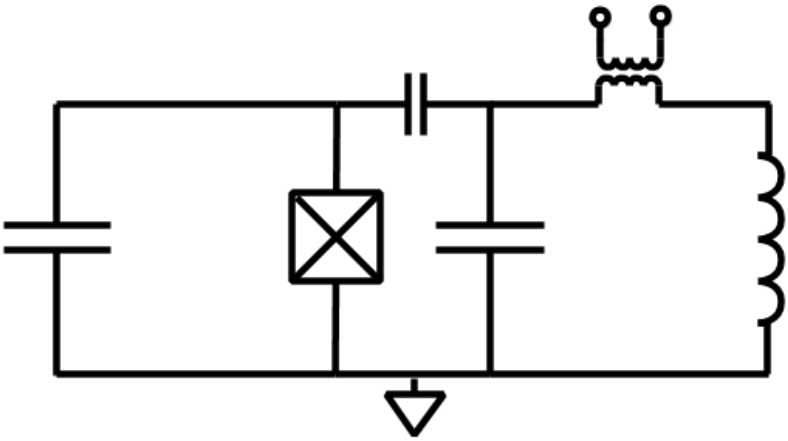

Figure 2.5: The capacatively coupled qubit-resonator system used to realize the Jaynes-Cummings Hamiltonian for readout of the qubit.

frequency depending on the qubit state by $\chi \approx \frac{g^2}{\Delta}$.

2.5.1 Dispersive readout

We can rewrite the dispersive Jaynes-Cummings Hamiltonian equation 2.14, to show the shift in the qubit frequency:

$$\hat{H}_{JCd} = \frac{\hbar\omega_q'}{2}\hat{\sigma}_z + \hbar\hat{a}^\dagger\hat{a}(\omega_r' + \chi\hat{\sigma_z}). \tag{2.15}$$

This shift by χ can be used to readout the qubit state, since the cavity resonance frequency moves up by $2\hbar\chi$ when the qubit is excited. Measuring the cavity transmission at a given frequency, we can then infer the qubit state. This can be done by applying a microwave tone through a transmission line coupled to the resonator as seen schematically in figure 2.5.

This measurement is a quantum non-demolition measurement, which means that it projects the qubit state onto an eigenstate of $\hat{\sigma_z}$, but doesn't further disturb the qubit. This type of measurement is important since it does not just allow us to readout the qubit state, but also prepare the qubit state by either heralding the ground state or using feedback with single qubit gates.

When a qubit is coupled to a lossy cavity mode with decay rate κ, spontaneous decay is either enhanced or suppressed compared to when coupled to a continuum,

depending on whether the qubit is on or off resonance with the cavity mode [34]. This effect is known as the Purcell effect [34]. In the dispersive regime the decay rate can be expressed as

$$\gamma = \frac{g^2}{\Delta^2}\kappa. \tag{2.16}$$

When this decay rate is what limits the lifetime of a qubit, it is said that the lifetime is "Purcell limited". In order to have good readout fidelity and fast readout, it is necessary to have high enough coupling between resonator and qubit (high g) for a high dispersive shift high enough to distinguish the ground and excited state and to have a higher resonator-feedline coupling constant for a higher signal to noise ratio (this sets the external quality factor, and therefore the rate κ). This means there is a trade-off between readout speed and qubit lifetimes. This effect can be suppressed by using a Purcell filter, which can suppress Purcell decay while maintaining the rate of measurement[34].

2.6 Gates

2.6.1 Single qubit rotations

A pure state of a two level system is a vector on the surface of the Bloch sphere, which is a visual representation of the Hilbert space spanned by the states $|0\rangle$ and $|1\rangle$, and can be seen i Figure 2.6. In this picture unitary operations are rotations of the Bloch vector. To make a general rotation about the axis $\boldsymbol{n}$ by angle θ described by the rotation operator $R_x = e^{-\frac{\theta\hat{\boldsymbol{\sigma}}\cdot\mathbf{n}}{2}}$, where $\hat{\boldsymbol{\sigma}}$ is the Bloch vector, one can decompose the rotation into rotations around axes that are controlled experimentally.

Rotations around the x and y axis are done by applying a classical microwave drive with frequency ω_d to the qubits. With this the Hamiltonian can be written in terms of the generalized Rabi frequency $\Omega = \frac{2\xi g}{\Delta_d}$ where $\Delta_d = \omega_q - \omega_d$ and ξ is the drive strength,

$$\hat{H}_{JCdd} = \frac{\hbar\omega_q'}{2}\hat{\sigma}_z + \hbar\hat{a}^\dagger\hat{a}(\omega_r' + \chi\hat{\sigma_z}) + \hbar(\Omega^*\sigma_- + \Omega\sigma_+). \tag{2.17}$$

By choosing a frame rotating with the frequency of the microwave pulses, we see that we can make rotations around the x- and y-axis by choosing the phase of the

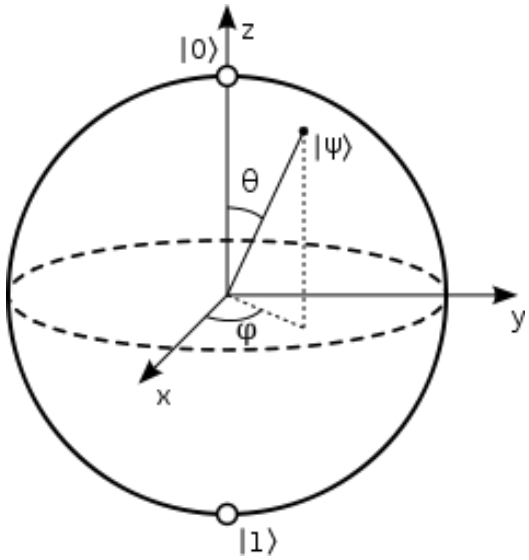

Figure 2.6: The Bloch sphere. The axis represent the expectation values of the Pauli operators. Single qubit operations correspond to rotations around these axes.

microwave pulse. The Hamiltonian becomes

$$\hat{H}_{JCdd} = \frac{\hbar\Delta}{2}\hat{\sigma}_z + \hbar\hat{a}^\dagger\hat{a}(\omega_r' - \omega_d + \chi\hat{\sigma_z}) + \hbar(\Omega_x\sigma_x + \Omega_y\sigma_y), \tag{2.18}$$

where $\Omega_x \cos(\omega_d t) + \Omega_y \sin(\omega_d t) = \Omega$.

To rotate about the z-axis, the gate is pulsed to adiabatically detune the qubit for some time to let it acquire a geometric phase. With this approach you can use the gate line for x- y- and z-control.

2.6.2 Two qubit gates

There are many different schemes for coupling qubits to each other for making gates. Capacitive coupling can be achieved by placing two qubit islands near each other, which gives rise to a mutual capacitance between the qubits. This is seen in figure 2.7. Capacitively coupling two transmon qubits will give rise to a coupling term in the Hamiltonian of the form

$$H_c = \hbar g_c \sigma_x^1 \sigma_x^2. \tag{2.19}$$

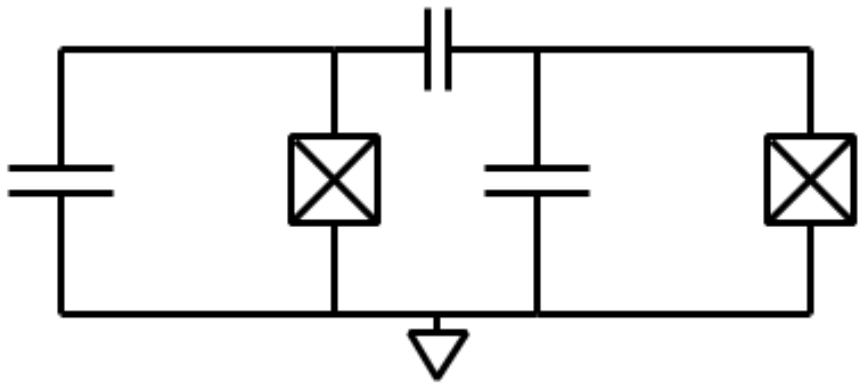

Figure 2.7: Two qubits capcacitively coupled.

Where the superscript refers to which qubit the Pauli operator acts on, and $g_c = \frac{1}{2\hbar}\sqrt{E_{01}^1 E_{01}^2}\frac{\sqrt{E_C^1 E_C^2}}{E_C^c}$ where E_C^c is the capacitive coupling energy [38]. In the RWA this Hamiltonian becomes

$$H_c = \hbar g_c(\sigma_+^1\sigma_-^2 + \sigma_-^1\sigma_+^2). \tag{2.20}$$

By tuning two capacitively coupled qubits into resonance for a time $t = \frac{\pi}{2g_c}$, one can do the $\sqrt{iSWAP}$ gate, which when combined with single qubit gates will form a universal gate set. The fidelity of this gate is limited by the fact that the transmon has negative anharmonicity, and the $|11\rangle$ state will go through an anticrossing with the $|02\rangle$ state when tuning the qubits into resonance, which means that the leakage out of the computational basis is given by the Landau-Zener formula.

Instead the gate used is the controlled phase ($C - phase$) gate [38]. This is achieved by using the same anticrossing that was a problem for implementing the $\sqrt{iSWAP}$ gate before. This is done by adiabatically pulsing one qubit to the frequency of the anticrossing with the $|02\rangle$ state for some time to let the $|11\rangle$ state acquire a phase of -1.

Chapter 3

Measurement setup

3.1 The dilution refrigerator

The samples need to be cooled down both to turn superconducting and to suppress thermal fluctuations at the qubit frequency, this means $hf \gg k_B T$ where ω is the frequency we operate the qubit at and T is the temperature of the sample. The qubits are operated at frequencies around 5 GHz while the base temperature of the fridge is around 25 mk.

All experiments were carried out in a Triton dry dilution refrigerator. The fridge is cooled to 4 K with pulse tube coolers, and the lowest stage where the sample is mounted reaches base temperature through a ^{3}He/^{4}He dilution process. Going from 4 K to base temperature there are a number of stages/plates with decreasing temperatures with each having a radiation shield to shield the stage underneath from black body radiation. Radio frequency (RF) coaxial cables as well as DC lines run through the fridge to control and readout the qubits. RF lines going through the fridge will carry Johnson noise from the equipment at room temperature (RT). To prevent this noise from reaching the sample a series of attenuators are installed inside the fridge. These also serve to thermalize the lines. All lines carrying RF to the sample are filtered with ECCOSORB®infrared filters. The lines carrying the readout pulses are additionally filtered with Marki low pass filter with a cutoff at 9.6GHz. The qubits have the control on a single combined RF/DC line with DC and and RF is combined in custom made bias-tees. Before

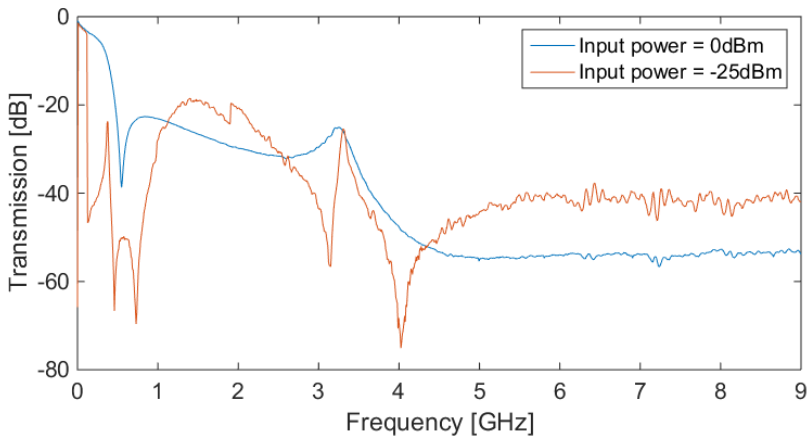

Figure 3.1: The transmission of a filter of the type used inside the bias tees at the fridge base temperature (25mK) applying respectively 0dBm and -25dBm of power through the filter.

the bias-tees, the DC signal is filtered through RC filters. The bias-tee enclosures include filters with reduced attenuation at frequencies below 300MHz.

It was recently discovered that at base temperature some components of these filters turn superconducting which changes the transmission of the filters if not enough power is applied to drive them into the normal state, which is around -15 dBm, much higher than the power used to drive the qubits. This can be seen in Figure 3.1. An attempt to fix this issue by gluing small NdFeB permanent magnets to the filters inside the bias-tee boxes was tested, but this did not eliminate the nonlinearity. All experiments done in this thesis were conducted with these nonlinear bias-tees and qubits were driven through the feed line rather than the control line.

The signal coming back from the sample is amplified twice; first by a travelling wave parametric amplifier (TWPA) [27] and then by a high electron mobility amplifier (HEMT). The TWPA is a near-quantum-limited amplifier with a 20dB gain in a band from 3 GHz to 8 GHz. It is mounted at base temperature in the fridge. To achieve parametric gain, a pump tone is applied through additional RF line with the same filtering as the line carrying the readout pulses. The pump and the readout signal are combined with a directional coupler. The values for

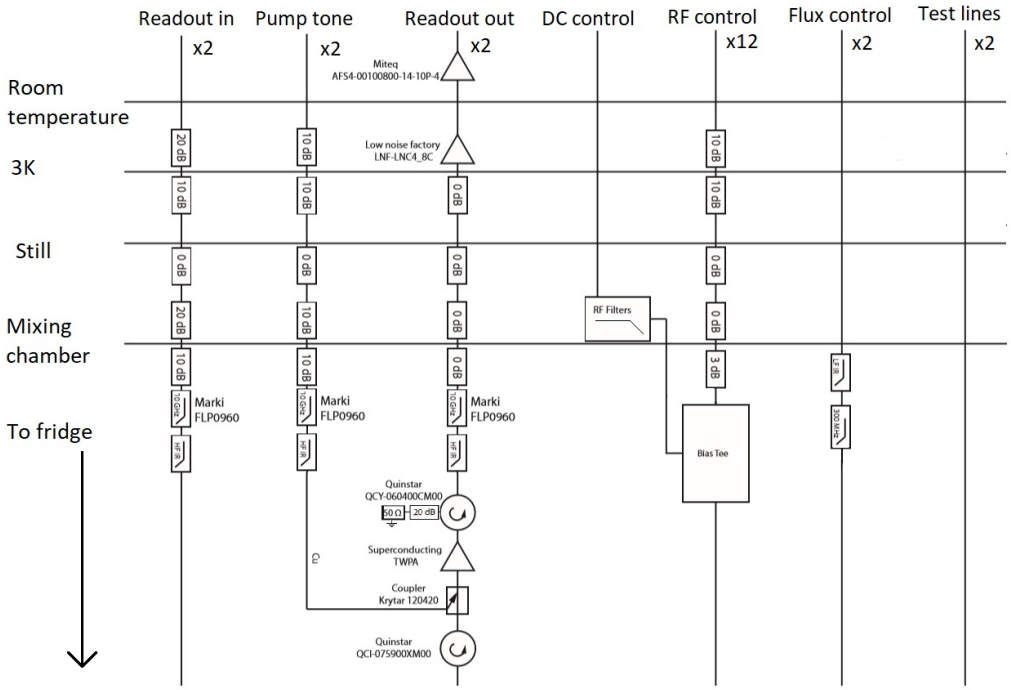

Figure 3.2: The setup of the electronics in the dilution refrigerator. This shows the readout circuits consisting of attenuated lines going to the sample, lines with amplifiers returning from the sample, and a pump. There the control lines combine RF and DC at bias-tees going to the sample. The fridge also has two flux lines for testing devices that require flux control and two unattenuated test lines.

the pump power and frequency are calibrated for the specific device. To prevent reflections in the amplifier chain from reaching the sample and the TWPA there are isolators after the sample and the TWPA. An isolator is a three port circulator with one port terminated with a 50Ω resistor to ground, so signal going in one port will go out the other, but signal going the other way will be terminated.

The HEMT amplifier is a low noise cryogenic amplifier that is mounted at 4K with 39 dB of gain from 4GHz to 8 GHz[25]. It is a transistor amplifier and therefore needs a DC voltage bias which is set and tuned at room temperature.

The fridge has a sample exchange system that allows one to exchange samples in the fridge without warming it up. This works by putting the samples inside a

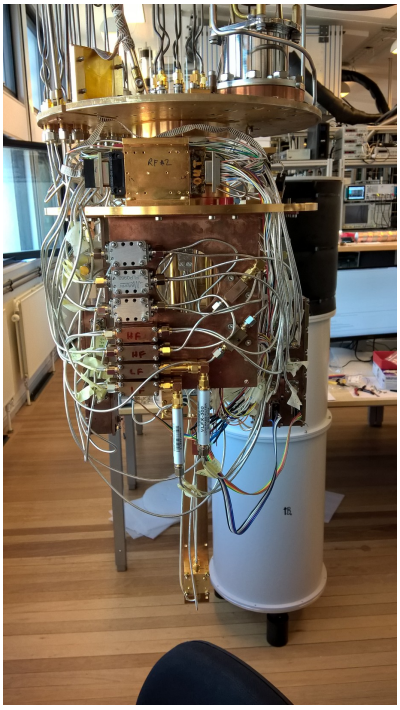

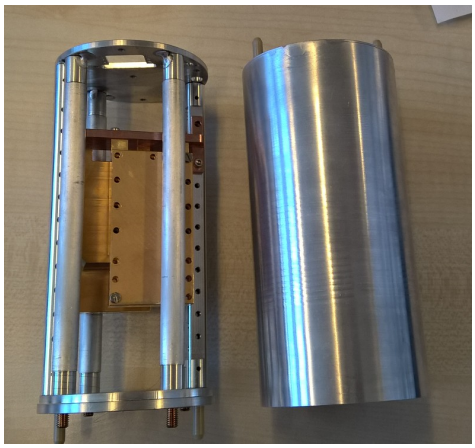

Figure 3.3: Right: The dilution refrigerator when opened. In this image the mixing chamber plate which will reach 25 mK when the fridge is running is shown with a custom made plate is mounted underneath. This plate is used to fit the bias tees and the filters that can be seen in mounted on a copper bracket. Before the fridge is closed, the TWPA will be mounted along with magnetic shields for the puck and TWPA. Left: The large puck that has two sample boxes in it. These can each be sealed with a sample in them with only coaxial lines going out.

puck which is loaded into the fridge from the bottom using a load lock, which can be mounted on the fridge and evacuated before opening a gate valve to the fridge. With this system the puck can be screwed into the coldfinger where SMP bullets from the puck engage with receptacles in the coldfinger to form an RF connection. Around the coldfinger where the puck is mounted is a cryogenic magnetic shield to shield the sample from magnetic fields. Inside the puck is an Al or Cu box with a custom made printed circuit board (PCB) onto which the chip itself is glued down with PMMA and wire bonded. The box has holes where RF coaxial cables go through but is sealed with an indium seal.

In a recent upgrade is set up so that two samples can be loaded and measured at once. This means that there has to be a readout circuit as described above for each sample. In this upgrade we also added more qubit control lines as well as lines with less filtering for control of devices that require flux bias. The coldfinger was upgraded to a larger one to fit the larger sample puck which holds two copper boxes each with a sample in it. This setup allows for parallel testing of devices. The fridge and puck is shown in Figure 3.3.

3.2 Room temperature electronics

Measurements done in this thesis fall in two categories: continuous wave (CW) and pulsed measurements.

For CW experiments we use a Rohde & Schwarz two port vector network analyzer (VNA) to measure scattering parameters. For measurements that require two tones a Rohde & Schwarz SGS 100A RF source is paired with the VNA.

to apply pulses we also use R&S SGS100A RF sources which have internal IQ mixers. The pulses are generated using a Tektronix AWG5014C arbitrary waveform generator (AWG). The pulses that drive the qubits can be applied through the feedline as well as through the qubit control lines. If the control pulses and the readout pulses both go through the feed line, the signals are combined by a power combiner before going into the fridge.

For reading out the qubit state, we use heterodyne detection with a local oscillator detuned by 12.5MHz. The intermediate signal is digitized with an Alazar ATS9360 digitizer card and mixed down to DC in software.

For setting the DC bias on the gate we use a custom multi channel DAC source or a Yokogava GS 200. A microwave switch is used to switch between pulsed and CW readout. All electronics equipment is controlled via either LAN or USB by a single computer and is, and RF instruments receive a 10MHz reference tone from a Rb clock source. Schematics of the room temperature setup can be found in Figure 3.2.

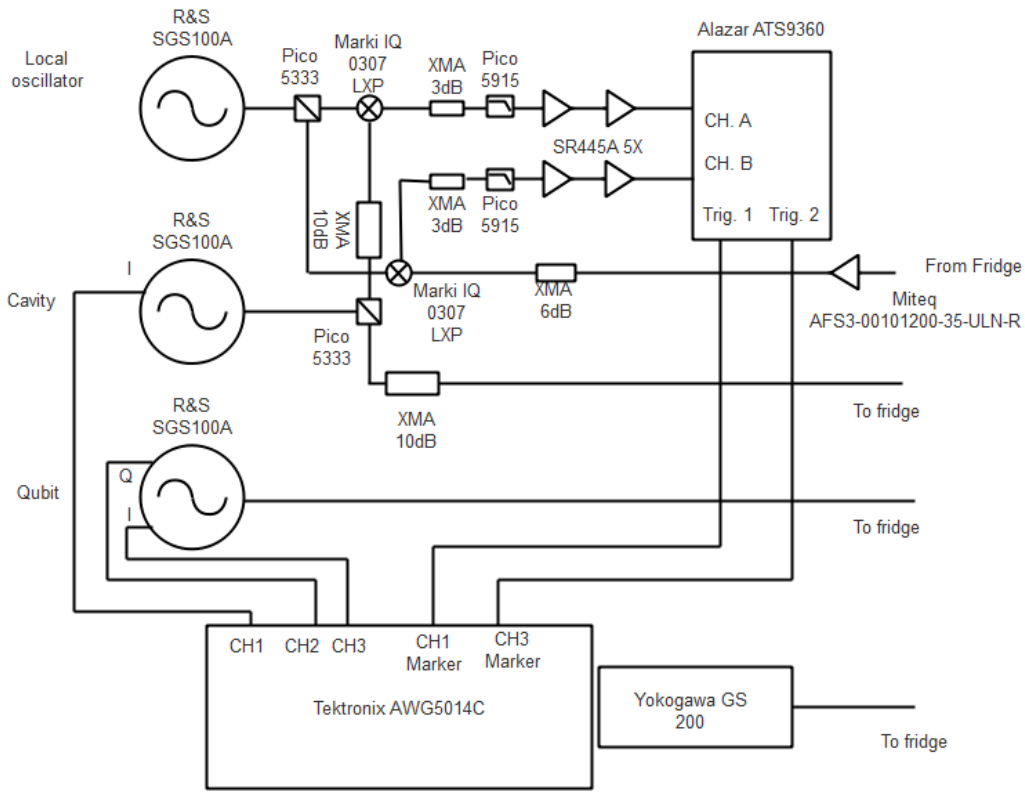

Figure 3.4: Schematic of microwave equipment setup at room temperature for control and readout of the qubit state. Using heterodyne detection the readout signal is mixed down to MHz frequencies before it is digitized. For control pulses, an RF source is modulated using an arbitrary waveform generator is used, and DC is applied using a voltage source.

Chapter 4

The sample

4.1 Design

All devices measured in this thesis are based on the same 6-qubit design, with different devices vary in materials and fabrication techniques used.

Each qubit is formed by an island made of aluminium surrounded by an aluminium ground plane. The island and the qubit are connected by a semiconductor JJ. The qubit capacitance to the ground plane is estimated from electrostatic simulations. The width and length of the junction are chosen to set the critical current, which seems to increase with wider junctions and decrease with longer junctions.

The qubit is capacitatively coupled to a transmission line resonator which is formed by a coplanar waveguide (CPW). The CPW is a waveguide that is formed on a dielectric substrate by a center conductor separated from the surrounding ground plane by two trenches as seen in Figure 4.1. The height of the trenches is negligible compared to the widths of the center conductor and the trench. To have a $\approx 50\ \Omega$ characteristic impedance, the width of the center conductor is twice that of the trenches. The speed of propagation of the signal is given by the effective permitivity of the CPW structure [35]

$$\epsilon_{eff} = \frac{\epsilon_r + 1}{2}, \tag{4.1}$$

where ϵ_r is the relative permitivity of the substrate. In our case the substrate is semi-insulating InP with $\epsilon_r = 12.1$ at microwave frequencies at low temperature

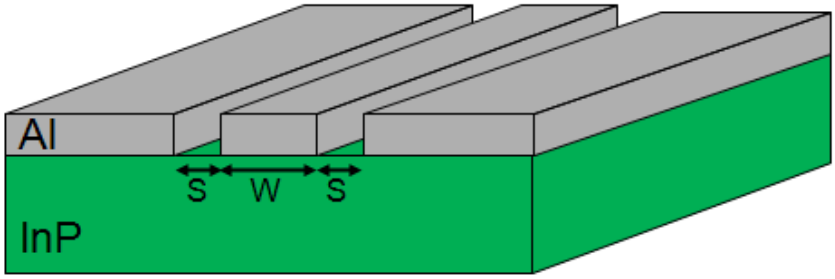

Figure 4.1: The coplanar waveguide geometry. A central conductor with width W is separated from a ground plane by two trenches of width S. The conductors are made form aluminium on an indium phosphide substrate.

[22]. The velocity of propagation then becomes

$$v_p = c\sqrt{\frac{2}{\epsilon_r + 1}}. \tag{4.2}$$

The transmission line resonators we use have one end open and one end grounded, this creates a quarter wave resonator, which has frequency

$$f = \frac{v_p}{4d} = \frac{c}{4d}\sqrt{\frac{2}{\epsilon_r + 1}} \tag{4.3}$$

Where d is the length of the resonator. A resonator with a frequency of 7GHz, which is roughly the frequency of the resonators in this thesis, the length of the resonator is roughly 4mm. To fit these on the chip, the feedline is meandered. At the end where the resonator is grounded, it couples inductively to a feed line. This is done by letting the end of the resonator run parallel to the feed line. The feed line is a CPW that couples to each of the readout cavities for dispersive readout. Each qubit has a control line carrying both AC and DC, this line ends as a topgate for the qubit junction. To connect to the PCB, the transmission lines have bond pads for wire bonding at the edges of the chips. The feedline also couples weakly to a test resonator which is used to determine the internal quality factor of the resonator. Qubits are placed next to each other so they couple capacitively to their

neighbour, which allows two qubits gates to be performed between qubits. The layout of the chip is shown in Figure 4.2.

4.2 Materials

The main difference between the two devices studied in this work is the materials used to make the superconductor-semiconductor junction. In one device a semiconductor hetrostructure hosting a two-dimensional electron gas (2DEG) with epitaxially grown Al is grown on the substrate, and the nanowire is defined by etching. On the other device, the nanowire is defined by selective area growth(SAG), and Al is grown everywhere on the chip.

The epitaxially grown Al gives a uniform clean interface with the semiconductor which allows the Al to induce a hard superconducting gap in the semiconductor through the proximity effect.

4.2.1 2DEG

The material used for the 2DEG device is grown on semi-insulating InP. The wafers used are Fe-doped semiinsulating InP, this reduces the conductivity which is necessary to reduce the currents induced in the substrate when making high Q transmission line resonators. On top of this is a buffer consisting of several different compound III-V semiconductor layers and then the 2DEG consisting of InAs sandwitched between two layers of InGaAs and finally a layer of Al. This stack is grown in an molecular beam epitaxy (MBE) chamber by growers at the Manfra group at Purdue University. This gives a high mobility 2DEG with superconducting Al on top. What becomes the nanowire is then later determined by two wet etch steps; one to remove the Al, and one to remove the 2DEG and buffer.

4.2.2 SAG

To pattern the SAG material it is grown with a mask of amorphous SiOx to determine where the growth happens. To make the, mask SiOx is deposited on the

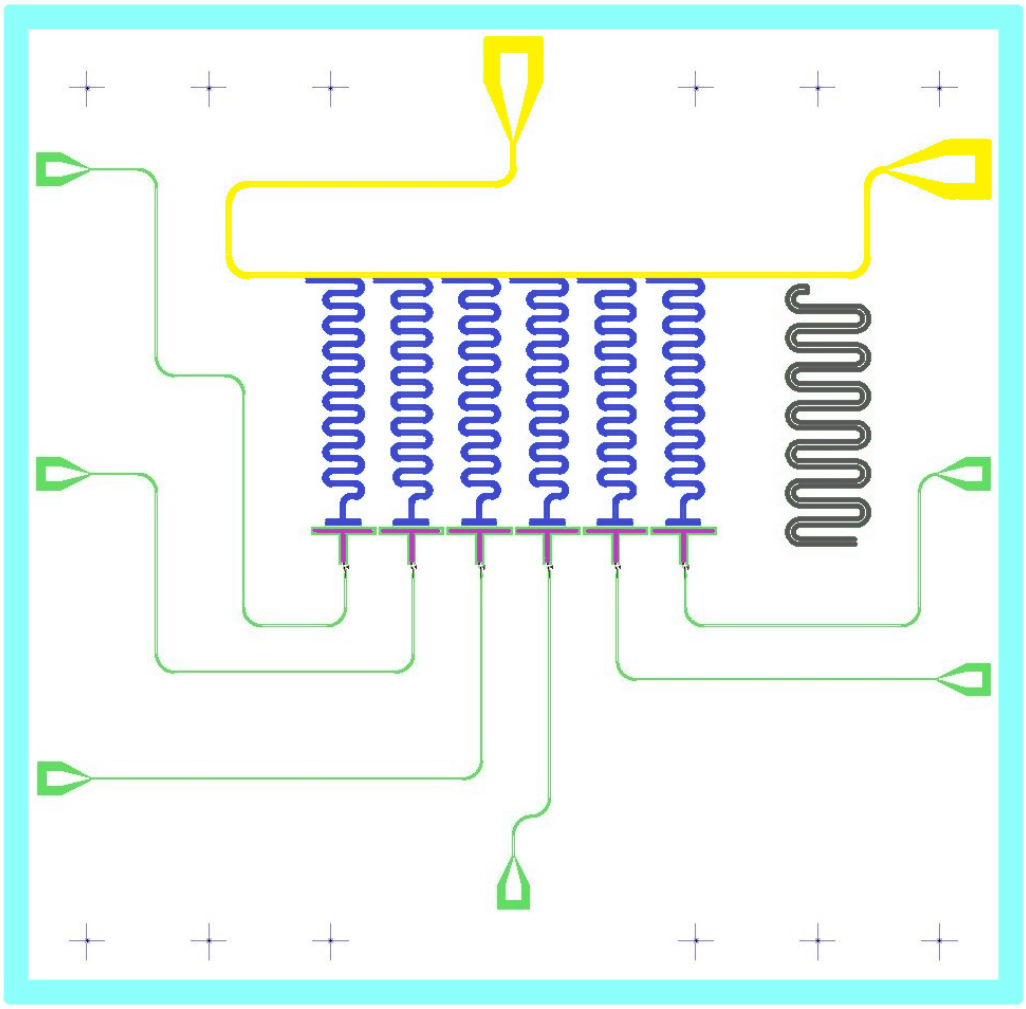

Figure 4.2: The layout of the chip. Qubit islands are T shaped and coulored green, the readout resonators are blue, the feedline is yellow, the control lines are green, and the test resonator is grey. The surrounding ground plane is white.

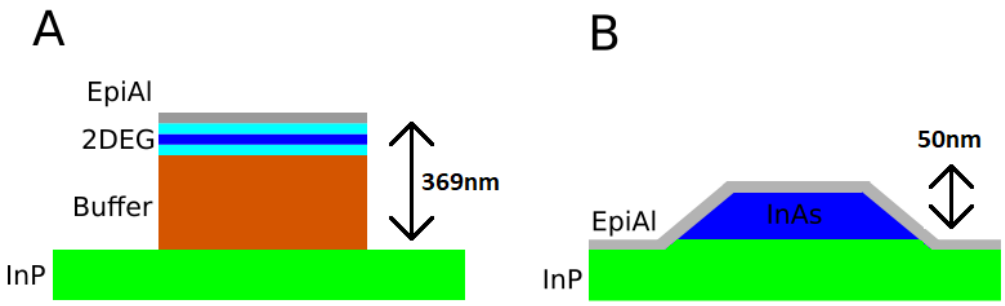

Figure 4.3: A) Profile of a nanowire etched etched out from a 2DEG. B) Profile of a nanowire grown by sellective area growth.

full wafer in a plasma-enhanced chemical vapor deposition system, then electron-beam lithography (EBL) is used to define etch windows and hydrofloric acid is used to etch growth windows in the SiOx. In the next step growers in at Scuola Normale Superiore in Pisa grow InP on the wafer and then InAs with MBE. Then the wafer is sent to Purdue where the mask is stripped with an HF dip and it is loaded into the MBE system for hydrogen assisted cleaning and then epitaxial Al is grown.

This results in an InP wafer with nanowires in the horizontal plane and Al which is in good electrical contact with the nanowires covering the whole wafer.

4.3 Fabrication

This section goes through the fabrication steps to make the two devices presented in this thesis. A number of other SAG devices were made, but either failed during the etch step and the fabrication was stopped, or they made it through, but did not yield any qubits we were able to coherently control. The complete recipes can be found in Appendix A and Appendix B.

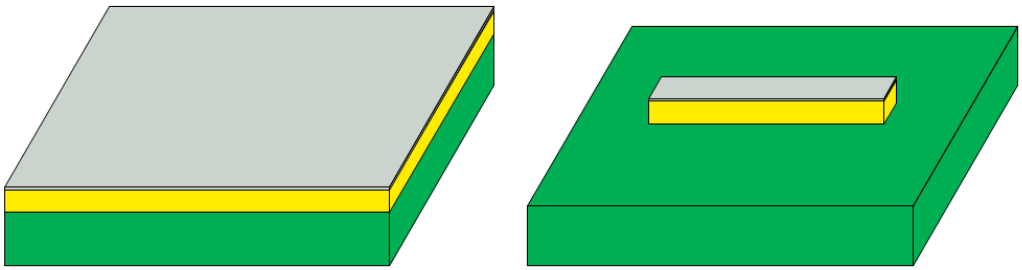

Figure 4.4: Left: The 2DEG material before fabrication has begun. Right: the device after the nanowire mesa etch. The InP substrate is illustrated in green and the semiconductor material is yellow and on the top is a layer of Al layer coulored grey.

4.3.1 2DEG

Alignment marks

To ensure allingment between different steps, Au alignment marks are deposited on the chip. The two nanolithography tools used; the Heidelberg μPG501 LED writer, and the Elionix ELS7000 EBL system, use these marks to allign the different layers. This step is done using a bilayer liftoff process with EBL, and evaporating 5 nm of Ti and 50nm of Au using an AJA thin film evaporation system. The alignment marks are cross shaped and Au is used because it can be seen well in electron microscopy.

Nanowire mesa etch

To define the nanowires, an etch process is used. To save time on the EBL system, we use a negative e-beam resist to cover the area where the nanowire is formed. Then the Al is etched away using Transene aluminium etchant type D, and then the 2DEG and buffer layer are etched using a III-V semiconductor etch solution. This leaves a behind a mesa structure that is in total 369nm tall on the substrate. This step can be seen in Figure 4.4.

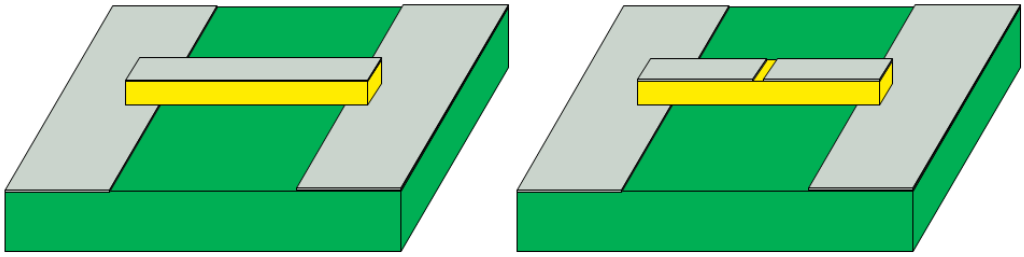

Figure 4.5: Left: The 2DEG device after the microwave control layer has been defined. Right: The device after the JJ has been etched out. The InP substrate is illustrated in green and the semiconductor material is yellow and Al has the color grey.

Microwave control

To make the microwave circuit on the chip, the nanowires are covered with a square of bilayer optical resist with the ends of the nanowire sticking out before 100nm of Al is evaporated on the chip, and the square is lifted off. The control circuitry is then patterned using optical lithography and etched using Al etchant type D. The reason for doing both a liftoff and an etch rather than just a single liftoff step is that the interface will be cleaner using the etch, which results in less loss, while the nanowire which is already there still needs to be protected with resist. This step is illustrated in Figure 4.5.

Junction etch

The JJ is made by etching away the Al on a section of the nanowire. This step is done using EBL and a wet etch with Al etchant. This step is illustrated in Figure 4.5.

Gate dielectric

The JJ is gated using a top gate this gate is separated from the JJ by a dielectric. This is done by opening up windows over the junction in a bilayer e-beam resist and depositing 25nm of HfO_2 using a Cambridge Savannah atomic layer deposi-

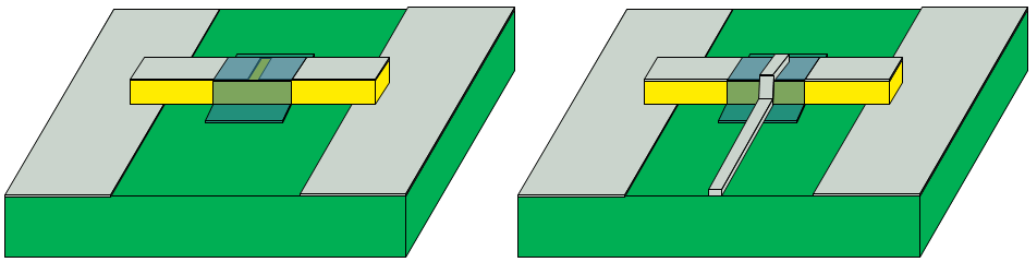

Figure 4.6: Left: The 2DEG device after atomic layer deposition. Right: The device after the electrostatic gate has been deposited. The InP substrate is illustrated in green and the semiconductor material is yellow, Al has the color grey and the HfOx is transparent blue.

tion system (ALD). This is followed by a liftoff with ultrasonication to remove sharp edges of the oxide, and it is annealed with forming gas at 150C for 30min. This step is illustrated in Figure 4.6.

Gates

The topgate are made using a bilayer liftoff process. 450nm of Al is evaporated to ensure it climbs up the mesa structure. The thick gates did not stick the first time they were deposited. This fabrication step was repeated with a 5nm layer of Ti underneath the 450nm of Al and the gates did stick. This step is illustrated in Figure 4.6.

Contacts

The final step in the process is contacting the nanowire and the gates. These contacts are made with a bilayer liftoff and Kaufman milling to make electrical contact and depositing 450 nm of Al. This step is illustrated in Figure 4.7.

4.3.2 SAG

Al etch

On this material, alignment marks are grown on the substrate along with the nanowires.

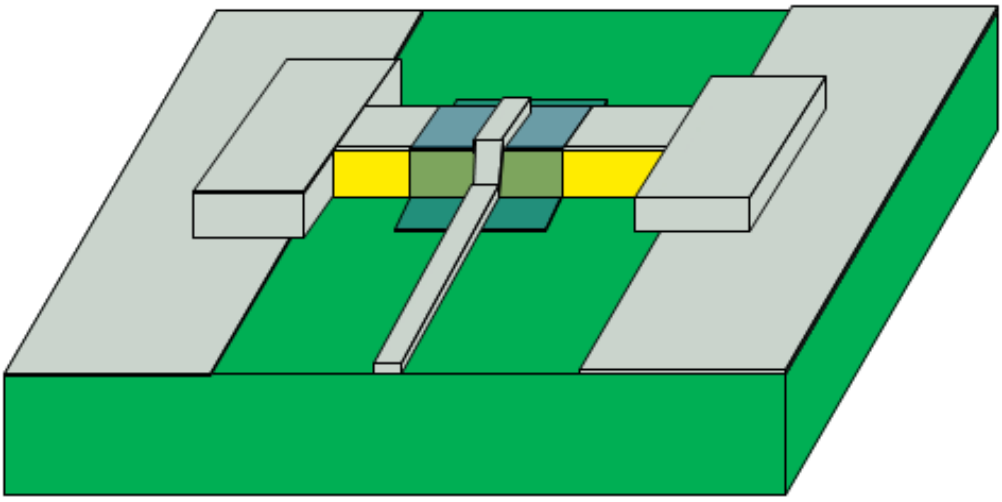

Figure 4.7: The finished 2DEG device after contacts have been made. The InP substrate is illustrated in green and the semiconductor material is yellow, Al has the color grey and the HfOx is transparent blue.

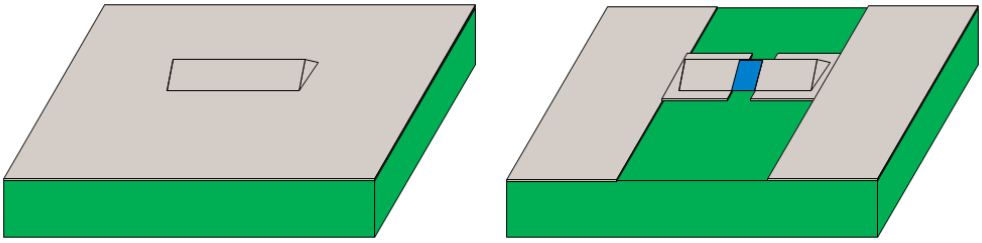

Figure 4.8: Left: The SAG material at the start of fabrication with the InP substrate in green and the nanowire under the Al which is grey. Right: The device after the JJ has been etched out.

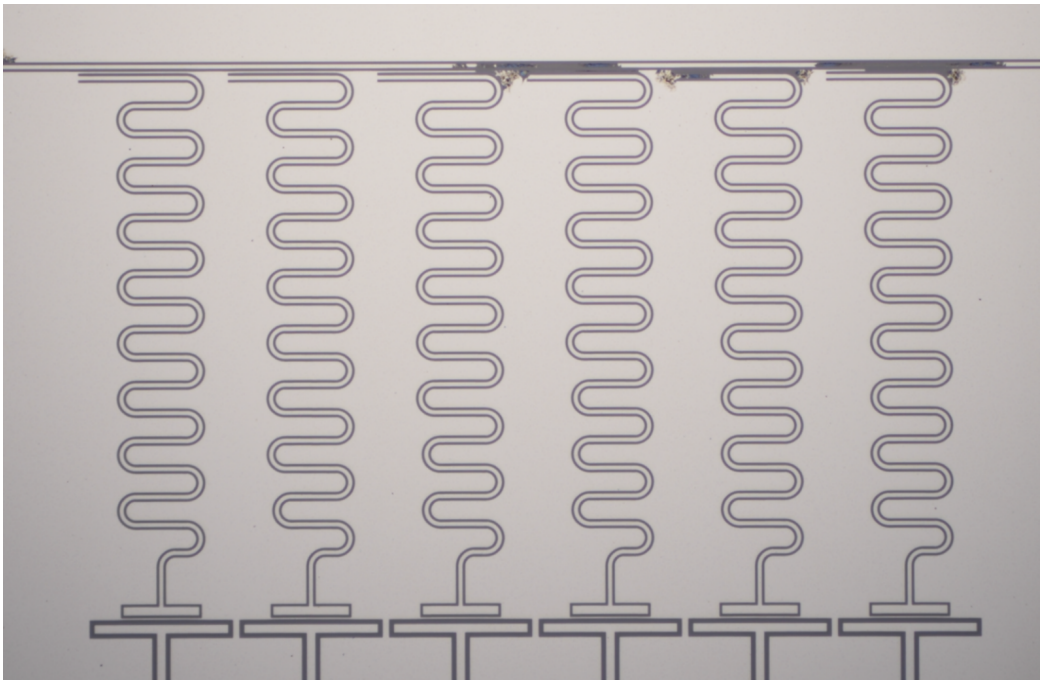

Figure 4.9: Optical micrograph taken after the Al etch. You can see run of the Al etchant under the resist causing some of the ground plane between the resonators and the feed line to be missing.

Since the material has epitaxial Al everywhere and nothing to etch away underneath, both the JJ and the microwave control circuit can be defined in a single etch. The mask is made with e-beam lithography using a low current to write the junction area and a larger current to write the coarser features of the microwave control. This is done using an Elionix ELS-F125 EBL system. The junction is etched using Al etchant type D. This is illustrated in Figure 4.8.

On this material the etchant ran under the resist for several of the devices we tried to fabricate. This was due to grains of Al on the sample. These grains in had nucleated on grains rich in indium on the substrate, which appeared after the hydrogen assisted cleaning procedure. The problem was eventually reduced by reducing the time of the hydrogen assisted cleaning step. A comparison between material with and without the hydrogen assisted cleaning procedure can be seen in Figure 4.10. On this device the etch ran, but the feedline and a qubit-resonator system was left intact, so fabrication was continued to the next step. This can be

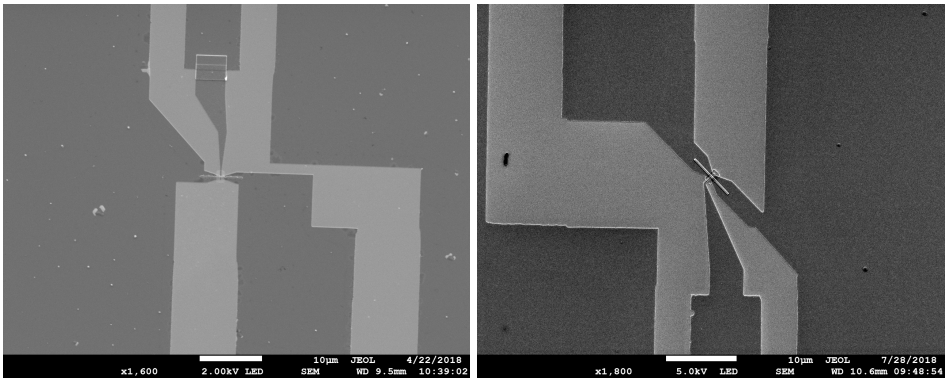

Figure 4.10: Right: SEM image taken using the JEOL 7800F of the area around a nanowire JJ on the SAG device. Left: SEM image of the area around a nanowire JJ fabricated on material that had not undergone the hydrogen assisted cleaning procedure. The grains can be seen in the H-cleaned device but not the device without the H-clean. The device without the H-cleaning has no contact patch, this is because it was fabricated using a newer fabrication procedure where the whole central conductor from the bondwire to the gate is deposited as a continuous piece of metal. This saves an EBL step.

seen in Figure 4.9.

Gate Dielectric

For this device, the gate dielectric was 15nm of HfO_2. It was deposited using a Cambridge Savannah ALD system. For this device the annealing was done after the depositions of the top gate, to test if this improved the dielectric. The annealing was done with forming gas for 30min at 150C. This is illustrated in Figure 4.11

Topgate

Due to the pyramid profile of the growth, there is no issue with the topgate climbing onto the nanowire. The topgate was deposited using a bilayer liftoff process with EBL, and the material was 50nm of evaporated Al with a 3nm Ti layer for sticking to the substrate. This is illustrated in Figure 4.11.

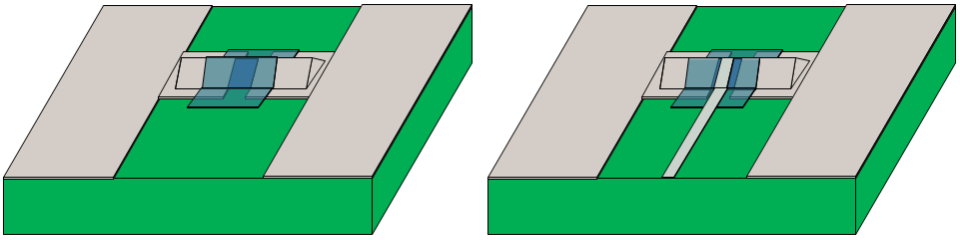

Figure 4.11: Left: The SAG device after the deposition of the gate dielectric. Right: The device after top gate deposition.

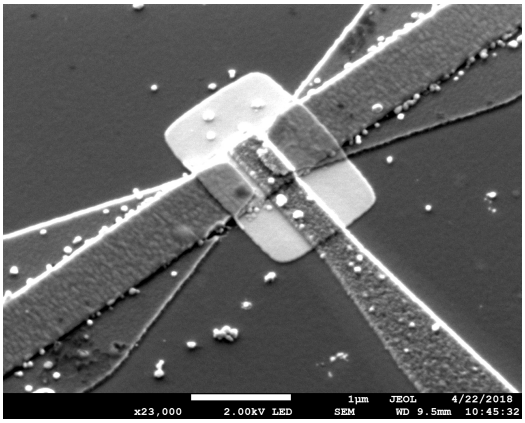

Figure 4.12: SEM image of josephson juncion made using a SAG nanowire and topgate. The grains in the picture are the same grains responsible for the failed etch.

Contacts

For the final step, contacts were made to the gates. This step was done with an EBL resist bilayer liftoff process with Kaufmann milling before deposition of 2nm of Ti and 50nm of Al.

Chapter 5

Measurements

This chapter explains the initial tuneup of the devices and goes on to characterization of qubits in terms of gateability, lifetimes, and coherence times. The measurements are done on the same two devices presented in the previous chapter.

5.1 Initial tuneup

When the device is at base temperature in the fridge, the first thing to do is locating the resonance frequencies of the readout resonators. This is done using a VNA to measure transmission through the feed line. The next thing to do is to look at the power dependence of the resonator frequency. At higher power the cavity is in the so called bright state [33], where the behaviour is that of a linear harmonic oscillator. As you go lower in measurement power, the cavity starts to behave non linearly due to the coupling to the qubit. Going further down in power, the cavity starts to behave as a harmonic oscillator with a qubit state dependent resonance frequency as described in section 2.5.1. This shift is approximately $\frac{g^2}{\Delta}$ in the dispersive regime. Seeing this power dependence is a good indication that what you are looking at is a resonator and qubit system. This allows you to choose a readout power that is low enough to see a linear cavity response, but not unnecessarily low, as the highest possible signal to noise ratio is still desired.

The next step is to use the electrostatic gate to see the avoided level crossing between the qubit and resonator. This is done by measuring the transmission of

the feed line while stepping the gate voltage. From the push on the cavity, one can make an estimate for the frequency knowing the designed qubit-resonator coupling. The coupling can vary from the designed coupling, since the devices are made using a wet etch, and the lateral undercut can vary from one fabrication run to the next.

The dispersive readout must then be calibrated. To do this, one can look at the magnitude of the cavity resonance, and pick a readout frequency on the side of the resonance where the slope is greatest. When the qubit is in the excited state, the resonator frequency will shift, and therefore the transmitted power at the chosen readout frequency will change. One thing dispersive readout can be used for is CW spectroscopy. Using a VNA and an external RF source, one tone is applied at the readout frequency, and one is swept in a chosen range. This can be used to find the qubit frequency, and at higher power a two-photon transition from the ground to second excited state can be seen, which can be used to find the anharmonicity of the qubit. Since the driving signal is always on, it is important to keep in mind, that a dynamic Stark shift appears [2]. Stepping the gate voltage while taking spectroscopy data allows one to map out the qubit frequency as a function of gate voltage. When this is done an automatic retuning of the readout is used since the Lamb shift changes when the qubit is moved with gate voltage.

With this information, it is possible to set the qubit at a chosen frequency. The qubit frequency is highly nonmonotonic as a function of gate voltage. This creates natural "sweet spots" where $\frac{\partial \omega_{01}}{\partial V_g} = 0$ and the qubit is therefore to first order insensitive to gate voltage noise [7]. The qubits are operated in the range from 3GHz to 5GHz where the coupling is strong enough to see a clear readout signal, but not so strong that the Purcell effect limits the lifetime of the qubit.

With a known qubit frequency you can drive Rabi oscillations in the qubit. This measurement, which is shown in Figure 5.7, is done by applying a pulse to drive the qubit, and afterwards a readout pulse to read out the qubit state. In these measurements, the qubit drive is applied through the feed line, but can just as well be applied through the dedicated control line. The frequency of the qubit drive is varied as well as either the length or the power of the drive pulse to vary the Rabi angle. The measured signal is acquired by averaging over many ($\tilde{1}000$) runs. The qubit is initialized by letting it decay into the ground state simply by waiting

a long time compared to the qubit lifetime before repeating the pulse sequence. From the Rabi oscillations one can find a power and pulse length for a π pulse and a $\frac{\pi}{2}$ pulse by finding the period of oscillation.

5.1.1 Lifetime and coherence time measurements

The qubit lifetime T_1 is the characteristic time of exponential decay from the excited state to the ground state. The measurement, which is shown in Figure 5.9, is done by applying a π pulse to the qubit in the ground state and waiting for a certain amount of time, and then reading out the qubit state. The signal is averaged over many runs, since we are looking for the excited state population. The waiting time is varied, and the qubit lifetime is determined by fitting an exponential decay to the averaged signal.

The coherence time or dephasing time of the qubit is known as T_2^* and is important for qubits as it sets the limit for how long information can be stored and processed during computation. T_2^* can be understood as the inhomogeneous dephasing time of an ensemble of measurements.

The coherence time is measured in a Ramsey experiment [37]. First a $\frac{\pi}{2}$ pulse is applied, this is followed by a pause, and then a second phase coherent $\frac{\pi}{2}$ pulse and finally readout. What happens can be understood by thinking of the Bloch sphere in a coordinate system rotating with the frequency of the applied π pulses. First the $\frac{\pi}{2}$ pulse will put the state on the equator of the Bloch sphere. In the time between pulses the Bloch vector will rotate due to the detuning of the pulse frequency from the qubit frequency. It is important, that the second pulse is phase coherent so it will rotate the Bloch vector around the same axis. This dephasing can be thought of in an ensemble average sense. When the qubit frequency fluctuates, the Bloch vector will process more or less from experiment to experiment and therefore the Bloch vectors will drift out of phase. Finally a readout pulse is applied. The averaged readout signal is plotted against the waiting time between pulses, giving damped oscillations known as Ramsey fringes. From a fit the exponential decay envelope T_2^* is found. The pulses applied to the qubits are shown schematically in Figure 5.1.

In the case for white noise Bloch-Redfield theory can be applied [17], in which

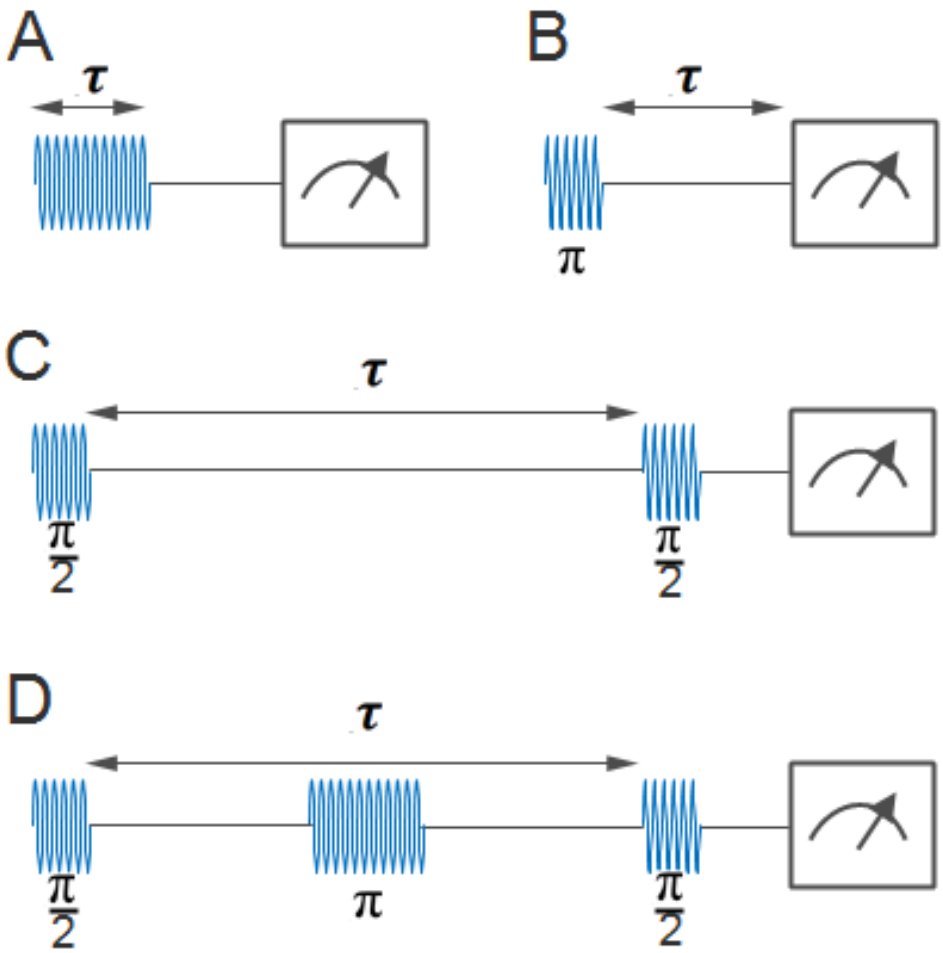

Figure 5.1: Pulses applied for different experiments. The box with the arrow at the end symbolizes a projective measurement of the qubit. In all the experiments the time τ is changed. A) Pulses used for Rabi oscillations. B) Pulses applied for measuring T_1. C) Pulses for measuring T_2^*. C) Pulses for measuring T_2^*.

the coherence time is combined of two rates; the rate of relaxation $\frac{1}{T_1}$ and the rate of pure depahsing $\frac{1}{T_2}$ In this model T_2^* can be expressed as

$$\frac{1}{T_2^*} = \frac{1}{2T_1} + \frac{1}{T_2}. \tag{5.1}$$

This means an upper limit on T_2^* is set by relaxation $T_2^* = 2T_1$.

In general, the noise in the qubit frequency is not white, but often has a $1/f$ spectral signature [26]. $1/f$ noise in the qubit transition frequency leads to a gaussian envelope form of the Ramsey fringes [40].

Low frequency noise can be corrected for by applying a so-called echo pulse [6]. This is a π pulse that is applied halfway between the two $\frac{\pi}{2}$ pulses. This pulse refocuses the Bloch vectors, and this means that at the time of the second pulse coherence is recovered. This gives an exponentially decaying readout signal, from which a characteristic time called T_2^{echo} is found.

T_1 T_2^* and T_2^{echo} depend on gate voltage and can also vary in time. The coherence time is in general higher at sweet spots [23].

5.2 Results

5.2.1 2DEG

The initial sweeps of gate voltage to find the anticrossing, showed the anticrossing at a voltage of around 0.17 V when sweeping both up and down. This can be seen in Figure 5.2.

The qubit transition appears in spectroscopy as either an increasing or decreasing signal depending on the chosen readout frequency relative to the cavity resonance and whether the qubit frequency is greater or less than the cavity frequency. A plot of the spectroscopy signal measured with a VNA can be seen in Figure 5.3. This shows the how the qubit frequency varies with gate voltage.

Measurements of T_1 T_2^* and T_2^{echo} can be found in Figures 5.4 with fits that determine the lifetime and coherence times. While no systematic study was conducted for the lifetimes and coherence times for the 2DEG device, typical measured values were $T_1 = 2\,\mu$s $T_2^* = 0.4\,\mu$s and $T_2^{echo} = 0.8\,\mu$ s.

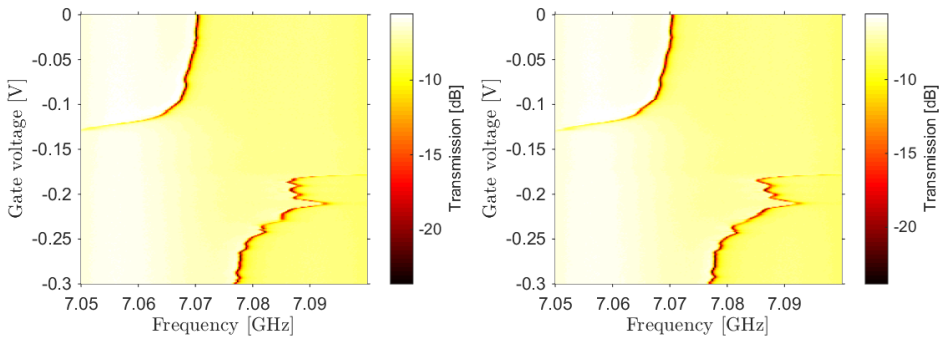

Figure 5.2: Right: Transmission of the feedline measured using a VNA while sweeping from positive voltages to negative voltages on the electrostatic gate of the qubit coupled a resonator coupled to the feedline. Left: Sweep from negative to positive voltage over the same range. This shows the qubit-resonator anticrossing. This data is taken with the 2DEG device showing very little hysteresis.

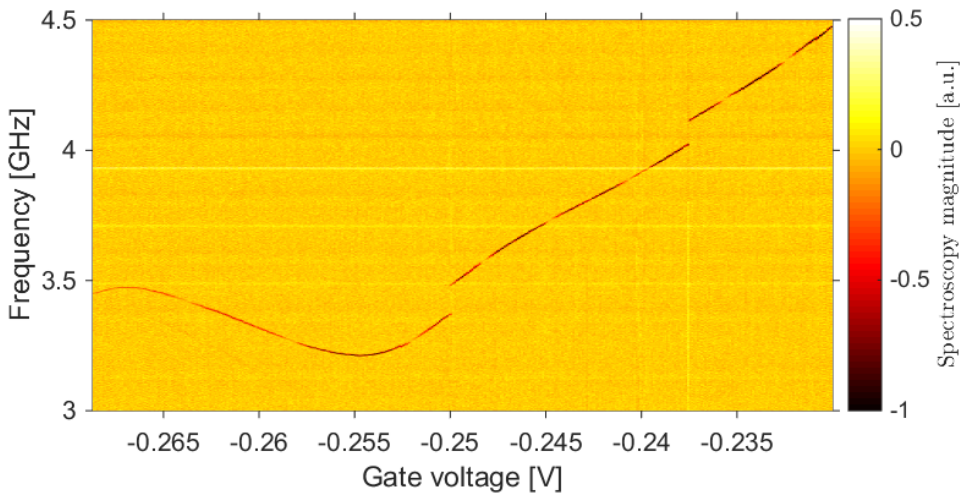

Figure 5.3: Two tone spectroscopy using a VNA and an external RF source used to determine how the 2DEG qubit frequency depends on the gate voltage. The peak can be seen as a red line and shows the qubit frequency moving with gate voltage.

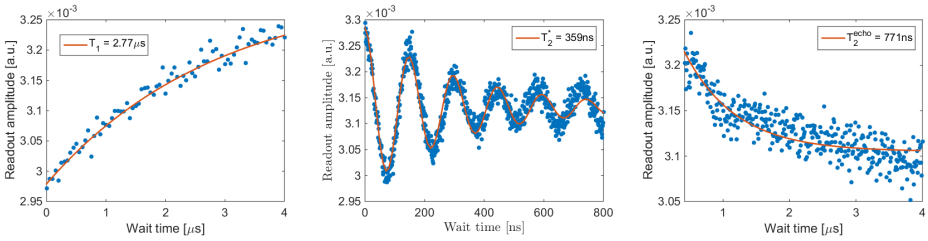

Figure 5.4: Lifetime and coherence time measurements of 2DEG qubits. The pulse schemes applied are shown in Figure 5.1. Readout is done using dispersive readout and averaged over many runs. Left: Lifetime measurement of 2DEG based qubit. The lifetime is inferred form the exponential fit to the data points shown. Center: Coherence time measurement of 2DEG qubit. The coherence time is inferred from fitting with a cosine with exponential decay. Right: T_2^{echo} measurement of the 2DEG based qubit. T_2^{echo} is inferred from an exponential fit.

5.2.2 SAG

Gate voltage sweeps while searching for the qubit-resonator anticrossing are shown in Figure 5.5. In the sweep from positive to negative gate voltages the anticrossing is at a higher gate voltage than in the sweep going from negative to positive voltages. This indicates that there is hysteresis in the qubit frequency.

The spectroscopy signal seen in Figure 5.6 was taken at a high drive power and with longer averaging time, since this qubit had a short lifetime, and the signal was therefore hard to see. This results in a readout signal where the $|0\rangle \rightarrow |2\rangle$ transition can also be seen, and because of the high averaging, the measurement took longer to take, and therefore more jumps in frequency can be seen.

It was possible to drive coherent oscillations in this device, the result of which can be found in Figure 5.7. These were driven by pulsing through the feedline using the pulse scheme shown in Figure 5.1 A. The lifetime of this qubit was measured to be $180ns$. The data taken as well as the fit to determine the lifetime can be seen in Figure 5.9. A measurement of the coherence time of the qubit was attempted, but it was not possible to measure T_2^*.

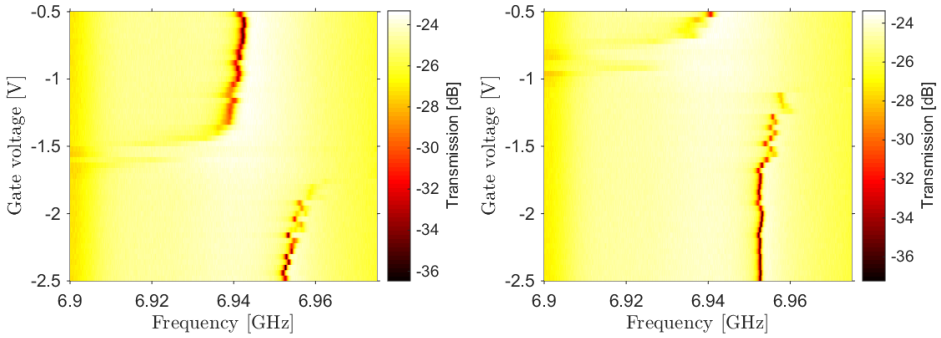

Figure 5.5: Right: Transmission of the feedline measured using a VNA while sweeping from positive voltages to negative voltages on the electrostatic gate of the qubit coupled a resonator coupled to the feedline. Left: Sweep from negative to positive voltage over the same range. This shows the qubit-resonator anticrossing. This data is taken with the SAG device showing significant hysteresis in the qubit frequency.

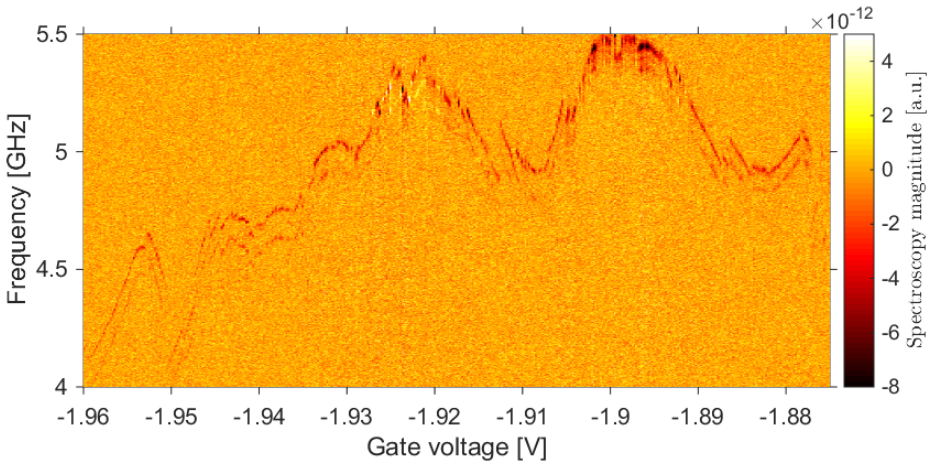

Figure 5.6: CW qubit spectroscopy used to determine how the SAG qubit frequency depends on the gate voltage. Two peaks following each other are seen in this is the $|0\rangle \rightarrow |1\rangle$ and the $|0\rangle \rightarrow |2\rangle$ transitions. These are seen because the drive power had to be high to see the $|0\rangle \rightarrow |1\rangle$ transition.

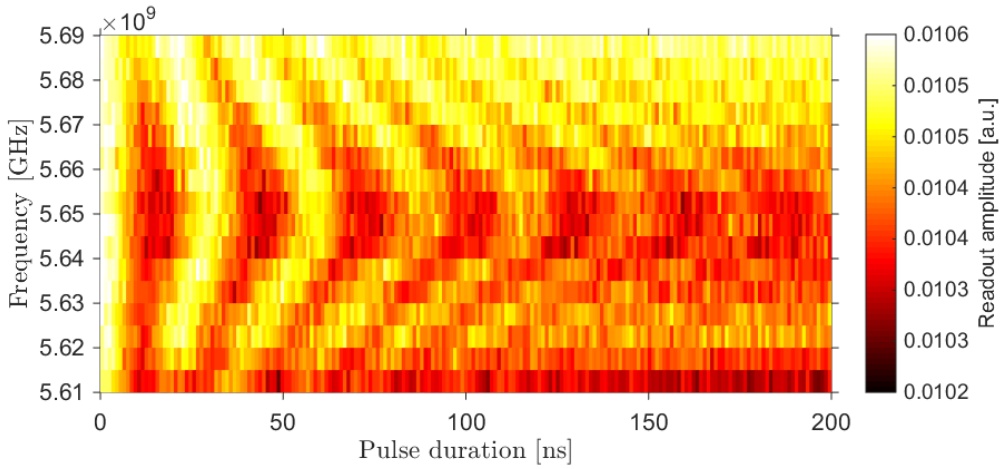

Figure 5.7: Coherent oscillations in SAG qubit. The Rabi angle is swept by sweeping the time of pulses applied to the qubit and by sweeping the drive frequency along the other axis. A horizontal linecut is shown in Figure 5.8

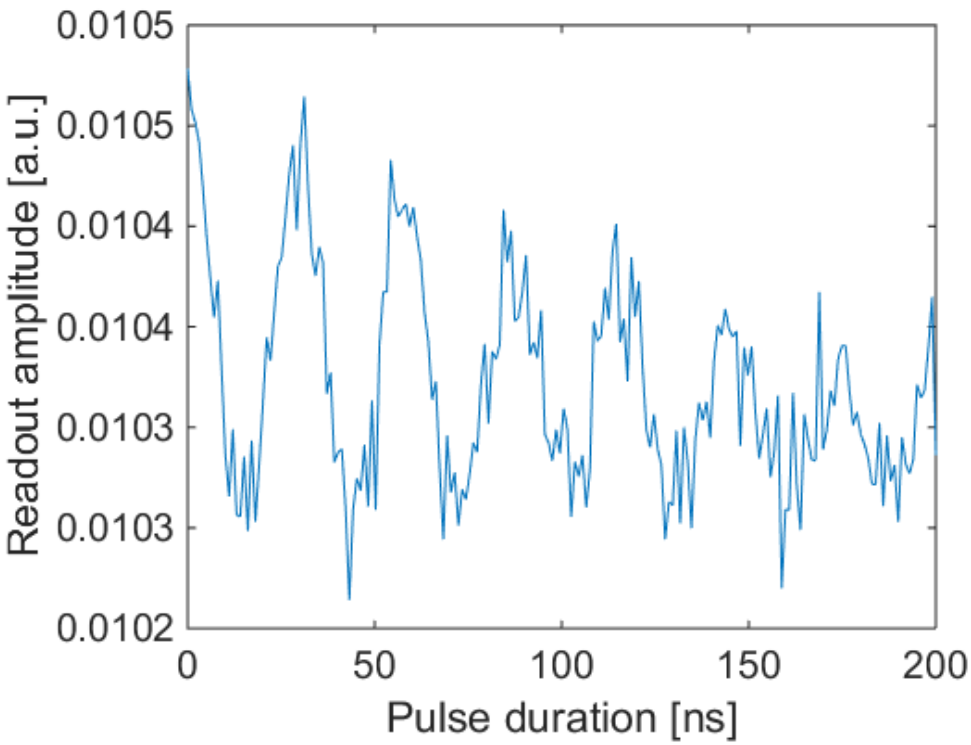

Figure 5.8: Linecut of Figure 5.7 showing the Rabi oscillations. The drive is on resonance with the qubit frequency.

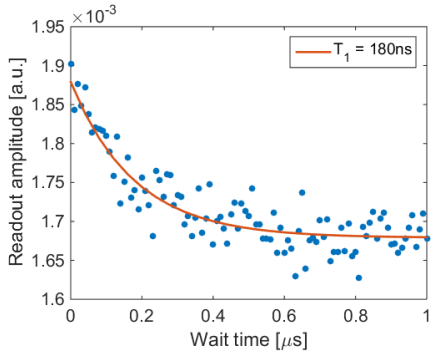

Figure 5.9: Lifetime measurement of a SAG qubit. The pulse scheme applied is as seen in Figure 5.1. The lifetime of the qubit is determined by fitting with an exponential decay model. Data is acquired using dispersive readout and each data point is averaged over many runs ≈ 1000

5.3 Discussion

Hysteresis and drift or discrete jumps in qubit frequency present a problem for operating qubits when one wants to run computations on a quantum computer, as the qubit frequency must be well known and controlled. The problem of hysteresis seems to consistently appear in these top gated devices. To improve this one would have to look at electrical environment of the JJ. This could be done by improving the interfaces by changing the fabrication procedure and the quality of the gate dielectric by changing the recipe for deposition and annealing. The hysteresis is more pronounced in the SAG devices, for which a different oxide thickness and deposition temperature was used.

In the spectroscopy date Figure 5.3 horizontal lines in the spectroscopy signal as well as points where the peak disappears. This could be attributed to resonant modes on the chip due to the ground plane being divided into smaller sections. These on-chip modes can be harmful to readout as well as the qubit lifetime. To avoid these modes crossover metal bridges that go over the transmission lines and connect the different sections of the ground plane to form a single ground plane could be included in the device design [13] [10].

The fluctuations in the qubit frequency as a function of gate voltage as seen in Figures 5.3 and 5.6 appear due to mesoscopic fluctuations in the disordered semi-

conductor region [3]. Although this gives sweet spots where the qubit frequency to first order does not depend on qubit frequency, it cannot be controlled where these appear, and they are therefore less useful for practical quantum computing.

The lifetimes and coherence times of the 2DEG device presented are similar to the device presented in [8]. Echo pulses were able to correct some of the dephasing, but not enough to reach $T_2^{echo} \approx 2T_1$ suggesting that low frequency noise is present, but does not fully account for the decoherence in these qubits. What is new in this device is the fabrication procedure in which the microwave control layer which takes up a large area of the chip is written with UV lithography. This reduces the time it takes to fabricate these devices, which is useful when making many devices to test the effects of adjustments to the fabrication technique.

It was not possible to measure the T_2^* of the SAG device. This could be due to the T_2^* being too low to measure. Since the test resonator in the device design did not survive the etch running under the resist, it was not possible to get a measurement of the internal quality factor, which can give information about the dielectric loss in these devices. The fact that the lifetime was much longer in the 2DEG qubits than the SAG qubits, indicates that dielectric loss is not what limits T_2^*. Many other SAG devices were fabricated, but none of these we were able to drive Rabi oscillations like in this one.

It is possible that the low lifetime of these qubits was due to a soft superconducting gap. In the fabrication of the previous versions of the gatemon, the Al was grown after the semiconductor material without leaving the MBE chamber. In these devices, the material is deposited after the substrate has been taken out of the MBE chamber and has had the SiOx layer removed with a hydrofloric acid etch before it is loaded into the MBE where it goes through the hydrogen assisted cleaning procedure and the Al is grown. This could result in a lower quality of the interface between the superconductor and the semiconductor. This could lead to subgap conductance, which could be what is limiting T_1.

In [8] it was concluded that the limiting factor of the lifetime of the 2DEG gatemon is dielectric loss in the InP substrate. While dielectric loss in InP at mK temperatures at microwave frequencies is not as well studied, it has been shown in [39] that the dielectric loss tangent of bulk Si is on the order of 10^{-6}, much less than that of the interfaces. Silicon is a material where high Q transmission

line resonators and have been demonstrated [5] [39] and VLS nanowire gatemon qubits reaching lifetimes of $20\,\mu$s have been realized [26]. Growth of InAs on a Si is possible using for example a Si/GaP template grown by metal-organic vapor phase epitaxy to start the growth on [11]. This could allow us to grow nanowires using SAG on a Si substrate to make qubits with lower dielectric loss.

Chapter 6

Conclusions and lookout

The fabrication and measurement of superconducting qubits based on semiconductor Josephson junctions called gatemons were carried out in this thesis. Two different fabrication techniques were explored, one of which was based on nanowires etched out from heterostructures hosting two dimensional electron gases, and the other is based on in situ grown horizontal nanowires using selective area growth. Both of these approaches solve a previous problem of nondeterministic fabrication when a VLS nanowire had to be transfered on to a new substrate.

Characterization of the qubits was carried out in a dilution refrigerator at 25 mK. This shows hysteresis in the qubit frequency when the electrostatic gate is swept as well as discrete jumps in the qubit frequency. The qubit frequency was mapped out as a function of gate voltage, and showed a nonmonotonic dependence with "sweet spots" where the qubit frequency to first order does not depend on the applied gate voltage. Measurements of lifetimes and coherences time are carried out giving $T_1 = 2\,\mu$s and $T_2^* = 0.4\,\mu$s for the 2DEG device, and $T_1 = 180$ ns with T_2^* being too short to measure.

These experiments showed the first demonstration of a qubit based on a selective area grown nanowire. While the lifetime and coherence time of this proof of concept device is short, improvements in the material quality and fabrication techniques could lead to improved qubit performance so these devices can be used as a saleable platform for quantum information processing.

To drive the qubits through the dedicated drive line which allows single line

control, the low pass filters inside the bias tees should be replaced with ones that don't turn superconducting at the fridge base temperature to avoid nonlinearities in the lines.

To improve the readout fidelity and lifetimes of these qubits crossover bridges going over the CPW on the chip to connect the ground plane could be implemented to avoid resonant on-chip modes. Purcell filters could also improve the readout fidelity without this limiting the qubit lifetime.

To improve the superconductor-semiconductor interface to ensure a hard superconducting gap, a process involving capping off the substrate with As after the growth of InAs to protect the interface could be explored. This layer would be evaporated from the sample when it is loaded into the MBE chamber before the Al growth. The hardness of the superconducting gap could then be directly probed in DC transport measurements.

To reduce dielectric loss on InP substrates a process for etching into the substrate displacing the substrate and the substrate-air interface away from high electric fields similar to [5] is currently being explored. Dielectric loss is then investigated by testing the Q-factor of superconducting transmission line resonators.

Finally an exciting direction is growth of SAG nanowires on silicon substrates. Si is a low loss substrate where gatemon qubits based on VLS nanowires have reached lifetimes of $20\,\mu$s. This could be a scaleable fabrication method to making gatemon qubits with long lifetimes.

Bibliography

[1] R. Barends, J. Kelly, A. Megrant, A. Veitia, D. Sank, E. Jeffrey, T. C. White, J. Mutus, A. G. Fowler, B. Campbell, Y. Chen, Z. Chen, B. Chiaro, A. Dunsworth, C. Neill, P. O'malley, P. Roushan, A. Vainsencher, J. Wenner, A. N. Korotkov, A. N. Cleland, and John M. Martinis. Superconducting quantum circuits at the surface code threshold for fault tolerance. *Nature*, 508(7497), 2014.

[2] M. Baur, S. Filipp, R. Bianchetti, J. M. Fink, M. Göppl, L. Steffen, P. J. Leek, A. Blais, and A. Wallraff. Measurement of autler-townes and mollow transitions in a strongly driven superconducting qubit. *Phys. Rev. Lett.*, 102:243602, Jun 2009.

[3] C. W. J. Beenakker. Universal limit of critical-current fluctuations in mesoscopic josephson junctions. *Phys. Rev. Lett.*, 67:3836–3839, Dec 1991.

[4] C. W. J. Beenakker. Three "universal" mesoscopic josephson effects. In Günther Bauer, Friedemar Kuchar, and Helmut Heinrich, editors, *Low-Dimensional Electronic Systems*, pages 78–82, Berlin, Heidelberg, 1992. Springer Berlin Heidelberg.

[5] A. Bruno, G. de Lange, S. Asaad, K. L. van Der Enden, N. K. Langford, and L. Dicarlo. Reducing intrinsic loss in superconducting resonators by surface treatment and deep etching of silicon substrates. *Applied Physics Letters*, 106(18), 2015.

[6] Jonas Bylander, Simon Gustavsson, Fei Yan, Fumiki Yoshihara, Khalil Harrabi, George Fitch, David G. Cory, Yasunobu Nakamura, Jaw-Shen Tsai,

and William D. Oliver. Noise spectroscopy through dynamical decoupling with a superconducting flux qubit. *Nature Physics*, 7(7), 2011.

[7] L. Casparis, T. W. Larsen, M. S. Olsen, F. Kuemmeth, P. Krogstrup, J. Nygård, K. D. Petersson, and C. M. Marcus. Gatemon benchmarking and two-qubit operations. *Phys. Rev. Lett.*, 116:150505, Apr 2016.

[8] Lucas Casparis, Malcolm R Connolly, Morten Kjaergaard, Natalie J Pearson, Anders Kringhøj, Thorvald W Larsen, Ferdinand Kuemmeth, Tiantian Wang, Candice Thomas, Sergei Gronin, Geoffrey C Gardner, Michael J Manfra, Charles M Marcus, and Karl D Petersson. Superconducting gatemon qubit based on a proximitized two-dimensional electron gas. *Nature nanotechnology*, 2018.

[9] W. Chang, S. M. Albrecht, T. S. Jespersen, F. Kuemmeth, P. Krogstrup, J. Nygård, and C. M. Marcus. Hard gap in epitaxial semiconductor–superconductor nanowires. *Nature Nanotechnology*, 273(5 Pt 1), 2015.

[10] Zijun Chen, A. Megrant, J. Kelly, R. Barends, J. Bochmann, Yu Chen, B. Chiaro, A. Dunsworth, E. Jeffrey, J. Y. Mutus, P. J. J. O'Malley, C. Neill, P. Roushan, D. Sank, A. Vainsencher, J. Wenner, T. C. White, A. N. Cleland, and John M. Martinis. Fabrication and characterization of aluminum airbridges for superconducting microwave circuits. *Applied Physics Letters*, 104(5), 2014.

[11] L. Desplanque, S. El Kazzi, C. Coinon, S. Ziegler, B. Kunert, A. Beyer, K. Volz, W. Stolz, Y. Wang, P. Ruterana, and X. Wallart. Monolithic integration of high electron mobility inas-based heterostructure on exact (001) silicon using a gasb/gap accommodation layer. *Applied Physics Letters*, 101(14), 2012.

[12] David P. Divincenzo. The physical implementation of quantum computation. *Fortschritte der Physik*, 48(9-11):771–783, September 2000.

[13] S. Filipp, M. Göppl, J. M. Fink, M. Baur, R. Bianchetti, L. Steffen, and A. Wallraff. Multi-mode mediated exchange coupling in cavity QED. *ArXiv e-prints*, November 2010.

[14] Jay M. Gambetta, Jerry M. Chow, and Matthias Steffen. Building logical qubits in a superconducting quantum computing system. *npj Quantum Information*, 3(1), 2017.

[15] Christopher C. Gerry and Peter L. Knoght. *Introductory Qauntum Optics*. Cambridge University Press, 2008.

[16] S M Girvin, M H Devoret, and R J Schoelkopf. Circuit qed and engineering charge based superconducting qubits. 2009.

[17] G. Ithier, E. Collin, P. Joyez, P. J. Meeson, D. Vion, D. Esteve, F. Chiarello, A. Shnirman, Y. Makhlin, J. Schriefl, and G. Schön. Decoherence in a superconducting quantum bit circuit. , 72(13):134519, October.

[18] Charles Kittel. *Introduction to Solid State Physics 7th ed.* Wiley, 1995.

[19] Jeffrey S Kline, Michael R Vissers, Fabio C S da Silva, David S Wisbey, Martin Weides, Terence J Weir, Benjamin Turek, Danielle A Braje, William D Oliver, Yoni Shalibo, Nadav Katz, Blake R Johnson, Thomas A Ohki, and David P Pappas. Sub-micrometer epitaxial josephson junctions for quantum circuits. *Superconductor Science and Technology*, 25(2), 2012.

[20] Jens Koch, Terri M. Yu, Jay Gambetta, A. A. Houck, D. I. Schuster, J. Majer, Alexandre Blais, M. H. Devoret, S. M. Girvin, and R. J. Schoelkopf. Charge-insensitive qubit design derived from the cooper pair box. *Phys. Rev. A*, 76:042319, Oct 2007.

[21] A. Kringhøj, L. Casparis, M. Hell, T. W. Larsen, F. Kuemmeth, M. Leijnse, K. Flensberg, P. Krogstrup, J. Nygård, K. D. Petersson, and C. M. Marcus. Anharmonicity of a superconducting qubit with a few-mode josephson junction. *Phys. Rev. B*, 97:060508, Feb 2018.

[22] Jerzy Krupka, John Hartnett, and Miroslaw Piersa. Permittivity and microwave absorption of semi-insulating inp at microwave frequencies. *Applied Physics Letters*, 98:112112–112112, 03 2011.

[23] T W Larsen, K D Petersson, F Kuemmeth, T S Jespersen, P Krogstrup, J Nygård, and C M Marcus. Semiconductor-nanowire-based superconducting qubit. *Physical review letters*, 115(12), 2015.

[24] H.W. Lenstra, J.P. Buhler, and C. Pomerance. Factoring integers with the number field sieve. *The development of the number field sieve (edited with A. K. Lenstra)*, 1993.

[25] Low Noise factory. *High electron mobility transistor LNF-LNC4_8C*, January 2018. Datasheet.

[26] F. Luthi, T. Stavenga, O. W. Enzing, A. Bruno, C. Dickel, N. K. Langford, M. A. Rol, T. S. Jespersen, J. Nygard, P. Krogstrup, and L. DiCarlo. Evolution of Nanowire Transmons and Their Quantum Coherence in Magnetic Field. *ArXiv e-prints*, November 2017.

[27] C Macklin, K O'Brien, D Hover, M E Schwartz, V Bolkhovsky, X Zhang, W D Oliver, and I Siddiqi. A near-quantum-limited josephson traveling-wave parametric amplifier. *Science (New York, N.Y.)*, 350(6258), October 2015.

[28] J. M. Martinis and K. Osborne. Superconducting Qubits and the Physics of Josephson Junctions. *eprint arXiv:cond-mat/0402415*, February 2004.

[29] J.M. Martinis, K.B. Cooper, R. McDermott, M. Steffen, M. Ansmann, K.D. Osborn, K. Cicak, S. Oh, D.P. Pappas, R.W. Simmonds, and C.C. Yu. Decoherence in josephson qubits from dielectric loss. *Physical Review Letters*, 95(21), 2005.

[30] W. L. McMillan. Tunneling model of the superconducting proximity effect. *Phys. Rev.*, 175:537–542, Nov 1968.

[31] Michael A. Nielsen and Isaac L. Chuang. *Quantum Computation and Quantum Information: 10th Anniversary Edition*. Cambridge University Press, New York, NY, USA, 10th edition, 2011.

[32] J. Preskill. *Lecture notes for physics 229: Quantum information and computation*. 1998/9.

[33] Matthew Reed. *Entanglement and Quantum Error Correction with Superconducting Qubits*. PhD thesis, Yale Univeristy, 2010.

[34] Eyob Sete, John M. Martinis, and Alexander Korotkov. Quantum theory of a bandpass purcell filter for qubit readout. *Physical Review A*, 92, 04 2015.

[35] Rainee N. Simons. *Coplanar Waveguide Circuits, Components, and Systems*. Wiley, 200.

[36] L. Tosi, C. Metzger, M. F. Goffman, C. Urbina, H. Pothier, S. Park, A. Levy Yeyati, J. Nygård, and P. Krogstrup. Spin-orbit splitting of Andreev states revealed by microwave spectroscopy. *ArXiv e-prints*, October 2018.

[37] D. Vion, A. Aassime, A. Cottet, P. Joyez, H. Pothier, C. Urbina, D. Esteve, and M. H. Devoret. Rabi oscillations, ramsey fringes and spin echoes in an electrical circuit. *Fortschritte der Physik*, 51(4-5):462–468, 2003.

[38] G Wendin. Quantum information processing with superconducting circuits: a review. *Reports on Progress in Physics*, 80(10):106001, 2017.

[39] W. Woods, G. Calusine, A. Melville, A. Sevi, E. Golden, D. K. Kim, D. Rosenberg, J. L. Yoder, and W. D. Oliver. Determining interface dielectric losses in superconducting coplanar waveguide resonators. *ArXiv e-prints*, August 2018.

[40] F. Yoshihara, K. Harrabi, A. O. Niskanen, Y. Nakamura, and J. S. Tsai. Decoherence of flux qubits due to $1/f$ flux noise. *Phys. Rev. Lett.*, 97:167001, Oct 2006.

Appendix A

SAG based gatemon fabrication recipe

A.1 Al etch

Resist
- Spin EL9, 4000rpm, 45s
- Bake for 2min at 115°C

Exposure
- Junction area
  - Write field size 300μm/60000 dots
  - Base dose: 320 μC/cm^2
  - Current 500pA
- Microwave control area
  - Write field size 600μm/20000 dots
  - Base dose: 320 μC/cm^2
  - Current 40nA

Development
- 30s MIBK:IPA 1:3
- 20s IPA

Ashing
- Oxygen plasma ashing for 1 min

Reflow – Bake for 1min at 125°C

Al-etch – 8s in Transcene D at 50°C
– 20s warm milli-Q water (MQ)
– 40s cold MQ

Strip resist – 5 min Dioxalane
– 2 min IPA

A.2 Gate dielectric

Resist – Spin El13, 4000rpm, 45s
– Bake 1min at 115°C
– Spin A4.5, 4000rpm, 45s
– Bake 1min at 115°C

exposure – Write field size 500μm/200000 dots
– Base dose: 900 μC/cm^2
– Current 3nA

Development – 60s MIBK:IPA 1:3
– 15s IPA

Ashing – Oxygen plasma ashing for 1 min

ALD – Deposit HfOx at 110 degrees, 150 cycles

Liftoff – Overnight dip in acetone
– inspection in IPA under microscope

Ashing – Oxygen plasma ashing for 2 min

A.3 Top Gate

Resist	– Spin El9, 4000rpm, 45s
	– Bake 1min at 115°C
	– Spin A4.5, 4000rpm, 45s
	– Bake 1min at 115°C
exposure	– Write field size 500μm/500000 dots
	– Base dose: 900 μC/cm^2
	– Current 3nA
Development	– 60s MIBK:IPA 1:3
	– 15s IPA
Ashing	– Oxygen plasma ashing for 1 min
Al deposition	– Kaufmann Milling at 0.4mTorr and 300eV for 4min 30s
	– evaporate 2nm of Ti
	– evaporate 150nm of Al
Liftoff	– 2hrs in acetone
	– inspection in IPA under microscope
Annealing	– Forming gas annealing 30min at 150 degrees

Appendix B

2DEG based gatemon fabrication recipe

B.1 Alignemnt marks

Resist	– Spin EL9, 4000rpm, 45s
	– Bake for 1min at 185°C
	– Spin A6, 4000rpm, 45s
	– Bake for 3min at 185°C
Exposure	– Write field size 300μm/20000 dots
	– Base dose: 826 μC/cm^2
	– Current 2nA
Development	– 80s MIBK:IPA 1:3
	– 15s IPA
Ashing	– Oxygen plasma ashing for 1 min
Evaporation	– 45 s Kauffman milling at 0.4mTorr and 300eV
	– Evaporate 5 nm Ti and 5o nm of gold
Liftoff	– overnight in acetone

- inspection in IPA under microscope

B.2 Nanowire mesa etch

Resist
- Spin AR 300 80 with 4000rpm for 45s
- Bake for 1min at 185°C
- 2 min in 1,3-dioxalane
- 1 min acetone
- 30 s IPA
- Spin AR 7520
- Bake for 1min at 85°C
- Spin AR 7520
- Bake for 1min at 85°C

Exposure
- Write field size 600μm/20000 dots
- Base dose: 75 μC/cm^2
- Current 1nA

Development
- 60s in MF321
- 60s in MQ

Ashing
- Oxygen plasma ashing for 2 min

Post-bake
- Bake for 1min at 115°C

Mesa etch
- III-V etch, use magnetic stirrer
  - 110ml MQ
  - 22.5ml citric acid
  - 1.5ml H_3OP_4
  - 1.5ml H_2O_2
- 13s in Transene D at 52°C

- 20s in 52°C warm MQ
- 20s in RT MQ
- 10 min in III-V etch
- 30 s in MQ

strip resist
- 2min 1,3 Dioxalane, sonication at 80kHz
- 2 min acetone
- 2 min IPA

Ashing
- Oxygen plasma ashing for 2 min

B.3 Microwave control

Resist
- Spin LOR3B
- bake 4 min at 185C
- Spin AZ1505,
- bake 2 min at 115C

Exposure (optical)
- expose pattern with UV for 23ms, full intensity

Develop
- 35s in MF321
- 5s in MQ

Ashing
- Oxygen plasma ashing for 2 min

Evaporation
- 30s Kauffman milling at 0.4mTorr and 300eV
- Evaporate 30nm of Al

Liftoff
- overnight in acetone
- inspection in IPA under microscope

Resist
- Spin on AZ1505 4000rpm 45s
- Bake 2 min at 115 degrees

Exposure (optical)
- expose pattern with UV for 23ms, full intensity

Development
- 60s in AZdeveloper
- 15s in MQ

Etch
- 33s in 52°C Transene D
- 1min in MQ

Strip resist
- 5 in in acetone
- 2min in IPA

B.4 Josephson junction

Resist
- Spin A4.5
- bake 3 min at 185C

Exposure
- Write field size 150μm/60000 dots
- Base dose: 75 μC/cm^2
- Current 500pA

Development
- 60s in MIBK:IPA 1:3
- 20s in MQ

Post bake
- Bake for 2 min at 115°C

Etch
- 33s in 50°C Transene D
- 20s in 50°C MQ
- 40s in RT MQ

Strip resist
- 5 min 1,3-dioxolane
- 2 min acetone
- 1 min IPA

B.5 ALD

Resist
- Spin EL9, 4000rpm, 45s
- Bake for 1min at 185°C
- Spin A6, 4000rpm, 45s
- Bake for 3min at 185°C

Exposure
- Write field size 150μm/60000 dots
- Base dose: 800 μC/cm^2
- Current 500pA

Development
- 60s MIBK:IPA 1:3
- 15s IPA

Ashing
- Oxygen plasma ashing for 1 min

ALD
- Deposit HfOx at 90 °, 250 cycles

Liftoff
- 4h in acetone
- Inspection in IPA

Annealing
- Forming gas annealing 30min at 150 degrees

B.6 Gates

Resist
- Spin EL9, 4000rpm, 45s
- Bake for 1min at 185°C
- Spin A6, 4000rpm, 45s
- Bake for 3min at 185°C

- Write field size 150μm/60000 dots
- Base dose: 826 μC/cm^2
- Current 500pA

Development
- 60s MIBK:IPA 1:3
- 15s IPA

Ashing
- Oxygen plasma ashing for 1 min

Al deposition
- evaporate 2nm of Ti
- evaporate 450nm of Al

Liftoff
- Liftoff in 1,3-dioxolane
- Inspect in IPA

B.7 Contacts

Resist
- Spin EL13, 4000rpm, 45s
- Bake for 1min at 185°C
- Spin A6, 4000rpm, 45s
- Bake for 3min at 185°C

- Write field size 150μm/60000 dots
- Base dose: 826 μC/cm^2
- Current 500pA

Development
- 60s MIBK:IPA 1:3
- 15s IPA

Ashing
- Oxygen plasma ashing for 1 min

Al deposition
- Kaufmann milling at 0.4mTorr and 300eV for 4m30s
- evaporate 2nm of Ti
- evaporate 450nm of Al

Liftoff
- Liftoff in 1,3-dioxolane
- Inspect in IPA